Emergence of a Nocturnal Low-Level Jet from a Broad Baroclinic Zone

ALAN SHAPIRO, a,b JOSHUA G. GEBAUER, AND DAVID B. PARSONS

^a School of Meteorology, University of Oklahoma, Norman, Oklahoma ^b Center for Analysis and Prediction of Storms, University of Oklahoma, Norman, Oklahoma ^c Earth Observing Laboratory, National Center for Environmental Research, Boulder, Colorado

(Manuscript received 15 July 2021, in final form 20 December 2021)

ABSTRACT: An analytical model is presented for the generation of a Blackadar-like nocturnal low-level jet in a broad baroclinic zone. The flow is forced from below (flat ground) by a surface buoyancy gradient and from above (free atmosphere) by a constant pressure gradient force. Diurnally varying mixing coefficients are specified to increase abruptly at sunrise and decrease abruptly at sunset. With attention restricted to a surface buoyancy that varies linearly with a horizontal coordinate, the Boussinesq-approximated equations of motion, thermal energy, and mass conservation reduce to a system of one-dimensional equations that can be solved analytically. Sensitivity tests with southerly jets suggest that (i) stronger jets are associated with larger decreases of the eddy viscosity at sunset (as in Blackadar theory); (ii) the night-time surface buoyancy gradient has little impact on jet strength; and (iii) for pure baroclinic forcing (no free-atmosphere geostrophic wind), the nighttime eddy diffusivity has little impact on jet strength, but the daytime eddy diffusivity is very important and has a larger impact than the daytime eddy viscosity. The model was applied to a jet that developed in fair weather conditions over the Great Plains from southern Texas to northern South Dakota on 1 May 2020. The ECMWF Reanalysis v5 (ERA5) for the afternoon prior to jet formation showed that a broad north–south-oriented baroclinic zone covered much of the region. The peak model-predicted winds were in good agreement with ERA5 winds and lidar data from the Atmospheric Radiation Measurement (ARM) Southern Great Plains (SGP) central facility in north-central Oklahoma.

KEYWORDS: Boundary layer; Jets; Mesoscale processes

1. Introduction

a. Overview of nocturnal low-level jets and their impacts

A common type of low-altitude wind maximum develops at night during the warm season in fair weather conditions after an afternoon of strong dry convective mixing. These nocturnal low-level jets (NLLJs) have been extensively documented over the Great Plains of the United States (Hoecker 1963, 1965; Bonner 1968; Parish et al. 1988; Stensrud 1996; Whiteman et al. 1997; Arritt et al. 1997; Banta et al. 2002; Song et al. 2005; Banta 2008; Walters et al. 2014; Parish and Oolman 2010; Berg et al. 2015; Parish 2016, 2017; Klein et al. 2016; Gebauer et al. 2018; Carroll et al. 2019; Smith et al. 2019; Bonin et al. 2020), but also occur in Australia, China, Russia, Germany, the Netherlands, Brazil, and many other countries (Sladkovic and Kanter 1977; Brook 1985; Van Ulden and Wieringa 1996; Stensrud 1996; Beyrich et al. 1997; Pham et al. 2008; Baas et al. 2009; Rife et al. 2010; Du et al. 2012, 2014; Kallistratova and Kouznetsov 2012; Fiedler et al. 2013; Oliveira et al. 2018). NLLJ winds typically peak in the 15–20 m s⁻¹ range, but can exceed 30 m s⁻¹. The jet usually attains peak intensity 0-3 h after local midnight, at heights less than 1 km above ground level (AGL), often less than 500 m AGL, and occasionally as low as ~100 m AGL. These winds typically have a dominant southerly component (over the Great Plains), but turn anticyclonically through the night. NLLJs arise from (or are at least heavily influenced by) the rapid decay of dry convective turbulence during the evening transition (Stull 1988),

Corresponding author: Alan Shapiro, ashapiro@ou.edu

possibly against a backdrop of baroclinic forcing, the subject of our study. NLLJs mix out during the morning transition, with the resumption of dry convective turbulence. We do not consider low-level wind maxima associated with coupled upper–lower-tropospheric jet streaks (Uccellini and Johnson 1979), surface cold fronts (Lackmann 2002), downslope wind-storms (Lilly 1978), gap winds (Macklin et al. 1990), or katabatic flows (Poulos and Zhong 2008).

NLLJs have numerous impacts on weather and climate. NLLJs can support and possibly initiate deep convection and heavy rains over the Great Plains by enhancing moisture transport and forcing ascent at the (typically) northern jet terminus (Trier and Parsons 1993; Stensrud 1996; Higgins et al. 1997; Arritt et al. 1997; Wu and Raman 1998; Walters and Winkler 2001; Tuttle and Davis 2006; Trier et al. 2006, 2014, 2017; French and Parker 2010; Weckwerth et al. 2019). NLLJenhanced convection along fronts also occurs in China, Argentina, and Brazil (Monaghan et al. 2010; Chen et al. 2017; Xue et al. 2018; Zeng et al. 2019; Du and Chen 2019). NLLJs can also support and possibly initiate convection along their lateral flanks (Walters and Winkler 2001; Reif and Bluestein 2017, 2018; Gebauer et al. 2018; Shapiro et al. 2018; Smith et al. 2019; Weckwerth et al. 2019; Parish et al. 2020), although the mechanism(s) for this phenomenon are not well understood. Air pollutants can be transported hundreds of kilometers by NLLJ winds before being mixed down to the surface during the morning transition (Corsmeier et al. 1997; Banta et al. 1998; Solomon et al. 2000; Mao and Talbot 2004; Bao et al. 2008; Klein et al. 2014; Sullivan et al. 2017; Miao et al. 2019). NLLJs also transport fungi, pollen, spores,

viruses, and insects (Drake and Farrow 1988; Wolf et al. 1990; Westbrook and Isard 1999; Isard and Gage 2001; Zhu et al. 2006; Westbrook 2008; Wainwright et al. 2020). During the North American spring, migratory birds use NLLJs as a flight aid (La Sorte et al. 2014; Wainwright et al. 2016; Shamoun-Baranes and Vansteelant 2017). NLLJs are an important source of wind energy (Cosack et al. 2007; Banta et al. 2008, 2013; Storm et al. 2009; Emeis 2013; Wilczak et al. 2019). During the morning transition, high momentum NLLJ air mixed down to the surface can intensify wildfires (Chandler et al. 1991; Dentoni et al. 2001; Charney et al. 2003; Lindley et al. 2019) and loft mineral dust (Washington and Todd 2005; Washington et al. 2006; Todd et al. 2008; Schepanski et al. 2009; Knippertz and Todd 2012; Heinold et al. 2013; Fiedler et al. 2013; Allen and Washington 2014; Ge et al. 2016; Vandenbussche et al. 2020).

b. Blackadar theory for the nocturnal low-level jet as an inertial oscillation

Many observational studies have attributed a major role in jet development to the Blackadar (1957, hereafter B57) conceptual model of the NLLJ as an inertial oscillation (IO) of the ageostrophic wind that is triggered by the shutdown of dry convective turbulence near sunset (Hoecker 1965; Brook 1985; Parish et al. 1988; Van Ulden and Wieringa 1996; Zhong et al. 1996; Andreas et al. 2000; Banta et al. 2002; Baas et al. 2009; Parish and Oolman 2010; Kallistratova and Kouznetsov 2012; Parish 2016, 2017; Parish and Clark 2017). B57 described the IO as an inviscid postsunset phenomenon for which the equations of motion admit a simple analytical solution. When plotted on a hodograph diagram, the velocity vector at any height traces an arc of a circle centered on the point representing the (assumed temporally constant) geostrophic wind at that height, with a radius equal to the initial (sunset) ageostrophic wind speed at that height. The velocity vector turns anticyclonically with time, and the speed peaks when the ageostrophic wind aligns with the geostrophic wind. For midlatitude IOs during the warm season, the speed maximum is predicted to occur within a few hours of (after) midnight.

Buajitti and Blackadar (1957) extended the B57 IO theory to include nighttime friction (turbulent stress), with a variety of time-height dependencies considered for the eddy viscosity. Solutions were obtained analytically for wind oscillations arising from an eddy viscosity that varied gradually over 24 h (single harmonic function of time), and numerically for oscillations arising from more realistic (rapid) decreases in eddy viscosity during the evening transition. However, as the computational grid had only five vertical levels, the numerically simulated flows were only coarsely resolved. Shapiro and Fedorovich (2010) solved the Navier–Stokes equations analytically for a viscosity that varied as a step function of time, with an abrupt decrease at sunset. The solution reproduced the main features of the Blackadar IO, but also displayed a strongly sheared layer adjacent to the ground within which the wind speed increased from zero to a low-altitude maximum. The peak winds were more intense and closer to the ground for larger ratios of daytime to nighttime viscosities. Van de Wiel et al. (2010) explored post-sunset IO-like solutions of an equation of motion in which the divergence of the turbulent stress was assumed to be temporally constant. The hodograph in that study depicted an undamped oscillation around a nocturnal equilibrium state. Smith et al. (2017) tested the analytical models of Shapiro and Fedorovich (2010) and Van de Wiel et al. (2010) using a direct numerical simulation (DNS) of a low-level jet over flat terrain. The two analytical solutions gradually diverged with time, with the quasi-spiral hodograph from the Shapiro and Fedorovich (2010) solution being in better agreement with the DNS.

c. Baroclinic nocturnal low-level jets

Although B57 did not explore the role of baroclinicity, the B57 discussion of their Fig. 10 makes clear that the basic IO theory also applies to the (baroclinic) case of a height-varying geostrophic wind. Interestingly, Buajitti and Blackadar (1957) attributed the large differences between winds in their numerical simulations and in their pibal data to deficiencies in the eddy viscosity specifications—even noting that the "distribution of eddy viscosity with height probably depends upon the temperature structure of the air mass"—but did not mention baroclinicity as a possible factor in the discrepancies.

To explain the geographical preference of the NLLJ over the southern Great Plains, Wexler (1961) hypothesized that the strong southerly current observed over that region during the warm season ("basic flow" on which the IO mechanism could operate) was generated by a deflection of trade winds by the Rocky Mountains in a manner similar to the Stommel mechanism for westward intensification of the Gulf Stream. However, according to Holton (1967), scale analysis of the governing equations showed that the Gulf Stream analog was not appropriate for the Great Plains NLLJ. Also in an attempt to understand the geographical preference for the NLLJ, Holton (1967) developed a one-dimensional (1D)¹ theory (in slope following coordinates) for oscillations of a viscous/diffusive fluid driven by a diurnally heated/cooled planar slope. The imposed surface (slope) buoyancy was temporally periodic but spatially constant. Horizontal vorticity was generated by virtue of air parcels near the slope being warmer or cooler than parcels in the free atmosphere at the same elevation. As the eddy viscosity and diffusivity did not vary with time, the IO mechanism could not operate. The diurnally varying slope buoyancy did induce wind oscillations, but the phase of the oscillations was not realistic, and the wind profiles were weak and not very jet-like. Shapiro et al. (2016, hereafter \$16) derived an analytical solution of the governing equations for wind oscillations over a slope that combined the main aspects of the Blackadar (diurnally varying mixing coefficients) and Holton (diurnally varying slope buoyancy) theories. In the unified theory, the Holton mechanism produced

¹ We describe a flow as one-dimensional (1D) if there is a coordinate system in which the velocity components vary in only one coordinate (height or slope-normal coordinate), regardless of the number of nonzero velocity components.

only weak wind maxima, but there was a synergistic effect when it acted in concert with the Blackadar mechanism (with the latter dominating).

The Holton (1967) slope-buoyancy theory is fairly restrictive, and other scenarios may be more relevant for baroclinic NLLJs. The slope buoyancies considered by Holton (1967) were (i) diurnally periodic about a zero mean, and (ii) spatially constant. Concerning (i), Bonner and Paegle (1970) showed that the southerly geostrophic wind over western Oklahoma and north-central Texas during a 1-week period in August 1960 was dominated by its mean, not by its diurnal variations. Additionally, Parish and Oolman (2010), Parish (2016, 2017), Parish and Clark (2017), and Parish et al. (2020) concluded that it was the strong warm-season mean southerly geostrophic wind over the southern Great Plains-not diurnal variations of the geostrophic wind—that promoted NLLJ development over the region. Concerning (ii), if the ground is flat, a spatially constant surface buoyancy cannot generate vorticity; a laterally varying buoyancy is needed to generate vorticity over flat terrain. Based on an analysis of 19 years of Oklahoma Mesonet data, Gebauer and Shapiro (2019) concluded that a mean warm-season westward-directed along-surface buoyancy gradient extended across Oklahoma and supported a strong southerly geostrophic wind at the surface, and that the contribution of the mean along-surface buoyancy gradient to that geostrophic wind was as important as the contribution by the diurnally heated slope. Several studies of Great Plains NLLJs have identified warm-air advection in westerly flow above the level of the wind maximum (Gebauer et al. 2018; Smith et al. 2019; Parsons et al. 2019; Parish et al. 2020), which is consistent with a westward increase in buoyancy over the region. It has long been recognized that sharp, nonlinear gradients in potential temperature and water vapor can occur over the sloping Great Plains during the warm season (e.g., Carlson and Ludlam 1968; Sun and Ogura 1979; Anthes et al. 1982; Benjamin and Carlson 1986; Parsons et al. 1991; Sun and Wu 1992). Carlson and Ludlam (1968) noted that intense thermal gradients could develop ahead of an approaching trough when moist air from the Gulf of Mexico collided with hot dry air that had descended from deserts to the west. Sun and Wu (1992) found that sloping terrain and strong westerly vertical shear were more important than the soil moisture gradient in creating a strong thermal gradient. It should be noted, however, that these studies focused on synoptic regimes that contained nonlinear thermodynamic gradients associated with drylines, and were often motivated by the need to understand the triggering of severe convection.

d. Outline of the study

We develop an analytical model for the generation of a Blackadar-like (though frictional) IO/NLLJ from a broad baroclinic zone over flat terrain. The starting point is the specification of a surface buoyancy that varies linearly with a horizontal coordinate (section 2). Spatial ansatzes for the dependent variables consistent with this form of surface

buoyancy reduce the Boussinesq-approximated equations of motion, thermal energy, and mass conservation to a system of 1D partial differential equations (section 2). The reduced equations are solved analytically in section 3. A reference run and sensitivity experiments are presented in section 4. In section 5, the model is applied to a baroclinic jet that developed over the Great Plains on 1 May 2020. The model winds are compared to output from the ECMWF Reanalysis v5 (ERA5) and Doppler lidar data from the Atmospheric Radiation Measurement (ARM) Southern Great Plains (SGP) central facility in north-central Oklahoma. Conclusions follow in section 6.

2. Problem formulation

We consider 1D flows forced from the ground (a horizontal surface) by a uniform horizontal buoyancy gradient, and from the free atmosphere by a uniform horizontal pressure gradient force (PGF). Diurnally varying eddy viscosity and diffusivity coefficients are specified to model (albeit crudely) the turbulent mixings of momentum and heat in the dry convective boundary layer, with a rapid decrease at sunset and a rapid increase at sunrise. Far above the surface, in the free atmosphere, the flow is barotropic and in geostrophic balance. In 1D theories for viscous/diffusive flow over a slope, a necessary condition for the existence of diurnally periodic solutions is that the free-atmosphere geostrophic wind is parallel to contours of terrain height (Holton 1967; S16). As there is no slope in the present study, there is no such restriction on the free-atmosphere geostrophic wind. With attention restricted to temporally periodic flows, there is no need to specify an initial state, and no spinup artifacts to contend with. As in Holton (1967) and \$16, a radiative damping term is included in the thermal energy equation.

We work in a right-handed Cartesian coordinate system (x, y, z) in which z is the vertical coordinate (ground is at z = 0), and the x axis is antiparallel to the along-surface buoyancy gradient, or antiparallel to that gradient during the daytime if it reverses during the 24-h period. This coordinate system reduces to the standard meteorological Cartesian system (x points eastward) when the surface buoyancy gradient points westward. The governing equations are the Boussinesq-approximated equations of motion, thermal energy and mass conservation (incompressibility condition), considered in their Reynolds-averaged forms:

$$\frac{\partial \mathbf{u}}{\partial t} + (\mathbf{u} \cdot \nabla)\mathbf{u} = -\nabla \Pi + b\mathbf{k} - f\mathbf{k} \times \mathbf{u} + \nu(t)\nabla^2 \mathbf{u}, \tag{1}$$

$$\frac{\partial b}{\partial t} + \mathbf{u} \cdot \nabla b = -N^2 w + \kappa(t) \nabla^2 b - \delta b, \tag{2}$$

$$\nabla \cdot \mathbf{u} = 0. \tag{3}$$

Here $u \equiv u\mathbf{i} + v\mathbf{j} + w\mathbf{k}$ is the velocity vector; \mathbf{i} , \mathbf{j} , and \mathbf{k} are the unit vectors parallel to the x, y, and z axes, respectively; u, v, and w are the x, y, and z components of velocity; $\nabla \equiv \mathbf{i}\partial/\partial x + \mathbf{j}\partial/\partial y + \mathbf{k}\partial/\partial z$; $b \equiv g[\theta_v - \Theta_v(z)]/\Theta_v(0)$ is buoyancy [g] is

acceleration due to gravity, θ_{v} is virtual potential temperature, $\Theta_{v}(z)$ is virtual potential temperature in a motionless reference atmosphere]; and $\Pi \equiv [p - P(z)]/\rho_c$ is the kinematic pressure perturbation [p] is pressure, P(z) is pressure in the reference atmosphere, and ρ_c is a constant reference value of density]. The radiative damping parameter δ (reciprocal damping time scale) in the radiative damping term $-\delta b$ in (2) is constant. With $\Theta_{v}(z)$ considered to vary linearly with z, the Brunt-Väsälä frequency $N = \sqrt{[g/\Theta_v(0)]}d\Theta_v/dz$ is constant. Since P(z) is independent of x and y, a freeatmosphere PGF and associated free-atmosphere geostrophic wind components u_g and v_g are specified through remote $(z \to \infty)$ conditions on $\partial \Pi/\partial x$ and $\partial \Pi/\partial y$. These remote components are spatially and temporally constant. The eddy viscosity ν and eddy diffusivity κ are functions of time, but independent of x, y, and z. They may be unequal. The Coriolis parameter f is constant.

As the surface buoyancy gradient is uniform and antiparallel to the x axis, we can write

$$\frac{\partial b}{\partial x}\Big|_{z=0} = b_{xs}(t), \quad \frac{\partial b}{\partial y}\Big|_{z=0} = 0,$$
 (4)

where $b_{xs} = (t)$ is a prescribed diurnally periodic function of time. Based on the forms of the governing equations, we anticipate that solutions exist in which the dependent variables satisfy the ansatzes:²

$$u = u_0(z, t), (5a)$$

$$v = v_0(z, t), \tag{5b}$$

$$b = b_0(z, t) + xb_x(z, t),$$
 (5c)

$$\Pi = \Pi_0(z, t) + x\Pi_x(z, t) + y\Pi_y(z, t), \tag{5d}$$

where u_0 , v_0 , b_0 , b_x , Π_0 , Π_x , and Π_y are independent of x and y. Since $\partial u/\partial x$ and $\partial v/\partial y$ are zero, integration of (3) with respect to z and application of the impermeability condition (w = 0 at z = 0) shows that w vanishes everywhere:

$$w = 0. (5e)$$

Differentiating (5c) and (5d) with respect to x, and (5d) with respect to y, yields $b_x = \partial b/\partial x$, $\Pi_x = \partial \Pi/\partial x$, and $\Pi_y = \partial \Pi/\partial y$. Applying (5c) and (5e) in the equation that results from taking $\partial/\partial y$ of the z-component of (1), yields $\partial \Pi_y/\partial z = 0$. Since Π_y is independent of z, the x component of the geostrophic wind is independent of z and is therefore equal to its

free-atmosphere value, u_g . In contrast, Π_x and the associated y-component geostrophic wind vary with z due to baroclinicity (thermal wind).

These ansatzes are similar to those in Gutman (1972, section 7.2), and we agree with Gutman's assessment that such ansatzes "can have physical meaning only at moderate x," since they preclude the horizontal convergence and accompanying vertical motion that would invariably arise near the ends of a more realistic surface thermal forcing of finite extent. These ansatzes may therefore be of more relevance for the broad baroclinic zone envisioned in our study than for the narrower zone of temperature contrasts more typical of a sea breeze or inland sea breeze. These ansatzes would also have limited applicability to a dryline, a narrow zone of strong temperature contrasts that develops internally on a slope (Parsons et al. 2000).

In view of (5a)–(5e), the incompressibility condition (3) is automatically satisfied, while (1) and (2) become

$$\frac{\partial u_0}{\partial t} = -\Pi_x + f u_0 + \nu(t) \frac{\partial^2 u_0}{\partial z^2},\tag{6}$$

$$\frac{\partial v_0}{\partial t} = -\Pi_y - f u_0 + \nu(t) \frac{\partial^2 v_0}{\partial z^2},\tag{7}$$

$$0 = -\frac{\partial \Pi_0}{\partial z} + b_0, \tag{8}$$

$$0 = -\frac{\partial \Pi_x}{\partial z} + b_x,\tag{9}$$

$$0 = -\frac{\partial \Pi_y}{\partial z},\tag{10}$$

$$\frac{\partial b_0}{\partial t} = -u_0 b_x + \kappa(t) \frac{\partial^2 b_0}{\partial z^2} - \delta b_0, \tag{11}$$

$$\frac{\partial b_x}{\partial t} = \kappa(t) \frac{\partial^2 b_x}{\partial z^2} - \delta b_x. \tag{12}$$

Thus, (5a)–(5e) have removed one dimension (x) from the governing equations, and rendered all but one of the non-linear terms [buoyancy advection term $-u_0b_x$ in (11)] identically zero. We refer to (6)–(12) as the reduced governing equations.

We seek periodic solutions of (6)–(12) subject to boundary condition (4), written as

$$b_x(0,t) = b_{xs}(t), \tag{13}$$

and the no-slip condition (u = v = 0 at z = 0), which becomes

$$u_0(0,t) = 0, \quad v_0(0,t) = 0.$$
 (14)

We omit descriptions of the lower boundary conditions for b_0 and Π_0 since those variables do not affect the wind field (section 3a), and we do not solve for them. The solutions of

² Restricting thermodynamic variables to vary linearly with a spatial coordinate has led to exact solutions of the nonlinear governing equations for sea breezes (Gutman 1972), motions due to thermocapillarity (Smith and Davis 1983a,b; Mercier and Normand 1996), thermal convection in a layer (Hart 1972; Aristov and Frik 1988; Ingel 1996; Fiedler 1999; Shvarts and Boudlal 2010; Medelfef et al. 2017), and katabatic flows on a differentially cooled slope (Shapiro and Fedorovich 2007).

(6)–(12) should also satisfy the remote (free-atmosphere) conditions:

$$\lim_{z \to \infty} u_0(z, t) = u_g, \quad \lim_{z \to \infty} v_0(z, t) = v_g, \tag{15a}$$

$$\lim_{z \to \infty} b_x(z, t) = 0, \quad \lim_{z \to \infty} b_0(z, t) = 0, \tag{15b}$$

$$\lim_{z \to \infty} \Pi_x = f v_g, \quad \lim_{z \to \infty} \Pi_y = -f u_g, \quad \lim_{z \to \infty} \Pi_0 = 0. \tag{15c}$$

Gutman (1972) solved a version of the reduced governing equations analytically for a diurnally varying surface buoyancy gradient. However, unlike the present study, Gutman did not consider planetary rotation, flow in the free atmosphere, a time dependence for ν or κ , or unequal values for ν and κ .

3. Analytical solution

The reduced governing equations are solved using the sequential procedure outlined in section 3a. Detailed derivations are given for the solutions of b_x (section 3b), Π_x (section 3c), and u_0 and u_0 (section 3d).

a. Overview of solution procedure

Step I: In view of (15c), integration of (10) produces

$$\Pi_{v} = -f u_{g}. \tag{16}$$

Step II: Solve (12) for b_x using the method of separation of variables subject to temporal periodicity and boundary conditions (13) and (15b). To contend with the time dependence in ν and κ , we use the orthogonal function expansion procedure developed in S16.

Step III: With b_x determined from step II, integrate (9) and use (15c) to obtain Π_x as

$$\Pi_x = f v_g - \int_z^\infty b_x(z', t) dz'. \tag{17}$$

Thus, the x-component PGF is due to (i) an impressing of the free-atmosphere PGF (expressed as fv_g) on the boundary layer, and (ii) a hydrostatic contribution by the horizontal buoyancy gradient.

Step IV: Applying (16) in (7), and (17) in (6), then multiplying (7) by the imaginary unit $i (\equiv \sqrt{-1})$, and adding the resulting equation to (6), yields an equation for the complex ageostrophic wind Γ (defined with respect to the free-atmosphere geostrophic wind):

$$\frac{\partial \Gamma}{\partial t} = -if \Gamma + \nu(t) \frac{\partial^2 \Gamma}{\partial z^2} + \int_z^\infty b_x(z', t) dz', \tag{18}$$

$$\Gamma \equiv u_0 - u_g + i(v_0 - v_g). \tag{19}$$

The procedure to solve (18) for Γ subject to temporal periodicity and boundary conditions (14) and (15a) is similar to that used to solve for b_x , but is more laborious because of the

complexity of the integral of b_x . Once Γ has been obtained, u_0 and u_0 follow from its real (\Re) and imaginary (\Im) parts as

$$u_0 = u_{\varrho} + \Re(\Gamma), \quad v_0 = v_{\varrho} + \Im(\Gamma).$$
 (20)

Step V: Although (11) is linear (with b_x and u_0 known from steps II and IV), its solution is made difficult by the complexity of the u_0b_x term. However, since b_0 does not affect the winds, it is of secondary interest, and we forego its solution.

Step VI: Integration of (8) with use of (15c) yields Π_0 as

$$\Pi_0 = -\int_{z}^{\infty} b_0(z', t) dz'.$$
 (21)

Like b_0 , Π_0 does not affect the wind field, and its evaluation is not pursued.

b. Solving for b_x

Substituting a trial solution for b_x in the separated variables form

$$b_x(z,t) = Z(z)T(t)$$
 (22)

into (12) produces

$$\frac{dT}{dt} = -\left[\delta - \sigma \kappa(t)\right]T,\tag{23}$$

$$\frac{d^2Z}{dz^2} - \sigma Z = 0, (24)$$

where σ is a separation constant. The general solutions of (23) and (24) yield b_x as

$$b_x = \text{const} \times e^{\pm z\sqrt{\sigma} - \delta t + \sigma \int_0^t \kappa(t')dt'}, \qquad (25)$$

where a prime denotes a dummy integration variable, and the \pm symbol indicates that a sign choice must be made to ensure that (15b) is satisfied. In view of (25), the periodicity condition $b_x(z, 0) = b_x(z, t_{24})$, where $t_{24} \equiv 24$ h, yields

$$1 = e^{-t_{24}(\delta - \sigma \overline{\kappa})}. (26)$$

where an overbar (of any variable) denotes the 24-h average of that variable, for example,

$$\overline{\kappa} \equiv \frac{1}{t_{24}} \int_0^{t_{24}} \kappa(t') dt'. \tag{27}$$

With the 1 in (26) written as $e^{2m\pi i}$ (m is an integer), we find that $-t_{24}(\delta - \sigma \overline{\kappa}) = 2m\pi i$, and thus obtain a distinct σ for each m as

$$\sigma_m = \frac{\delta}{\overline{\kappa}} + i \frac{2m\pi}{\overline{\kappa}t_{24}}.$$
 (28)

Generalized to include summation over m, (25) becomes

$$b_x = e^{-\delta[t-\eta(t)]} \sum_{m=-\infty}^{\infty} D_m F_m(t) e^{-z\sqrt{\sigma_m}},$$
 (29)

$$F_m(t) \equiv e^{2m\pi i \eta(t)/t_{24}},\tag{30}$$

$$\eta(t) \equiv \frac{1}{\kappa} \int_{0}^{t} \kappa(t')dt', \tag{31}$$

where D_m are unknown constants.

In arriving at (29), we have chosen the minus sign for the \pm symbol to ensure that $b_x \to 0$ as $z \to \infty$ since, as will now be shown, $\Re(\sqrt{\sigma_m}) > 0$ for all m. Setting $\sigma_m = R_m e^{i\Phi_m}$ in (28) yields $R_m \cos\Phi_m = \delta/\overline{\kappa}$ and $R_m \sin\Phi_m = 2m\pi/(\overline{\kappa}t_{24})$, from which we find that

$$R_m = \frac{\sqrt{\delta^2 + \left(2m\pi/t_{24}\right)^2}}{\overline{\kappa}},\tag{32}$$

 $\cos \Phi_m > 0$ for all m, $\sin \Phi_m$ has the same sign as m, and

$$\Phi_m = \tan^{-1} \left(\frac{2m\pi}{\delta t_{24}} \right), \tag{33}$$

where \tan^{-1} , the principal value of the inverse tangent, is between $-\pi/2$ and $\pi/2$. Since

$$\sqrt{\sigma_m} = R_m^{1/2} e^{i\Phi_m/2} = R_m^{1/2} \left[\cos\left(\frac{\Phi_m}{2}\right) + i \sin\left(\frac{\Phi_m}{2}\right) \right], \tag{34}$$

 $\Re(\sqrt{\sigma_m})$ has the sign of $\cos(\Phi_m/2)$. For m > 0, (33) yields Φ_m between 0 and $\pi/2$, so $0 < \Phi_m/2 < \pi/4$, $\cos(\Phi_m/2) > 0$, and $\Re(\sqrt{\sigma_m}) > 0$. For m < 0, Φ_m lies between 0 and $-\pi/2$, so $-\pi/4 < \Phi_m/2 < 0$, $\cos(\Phi_m/2) > 0$, and $\Re(\sqrt{\sigma_m})$ is again positive.

To determine D_m , apply (13) in (29) evaluated at z = 0, obtaining

$$\sum_{m=-\infty}^{\infty} D_m F_m(t) = b_{xs}(t) e^{\delta[t-\eta(t)]}.$$
 (35)

Multiplying (35) by $\kappa(t)F_n^*(t)$ (asterisk denotes complex conjugation), and integrating the resulting equation over 24 h using an orthogonality relation derived in S16:

$$\int_{0}^{t_{24}} \kappa(t') F_m(t') F_n^*(t') dt' = \delta_{mn} t_{24} \overline{\kappa}, \tag{36}$$

where δ_{mn} is the Kronecker delta, then yields

$$D_{m} = \frac{1}{t_{24}\overline{\kappa}} \int_{0}^{t_{24}} b_{xs}(t') \kappa(t') e^{\delta[t' - \eta(t')]} e^{-2m\pi i \eta(t')/t_{24}} dt'.$$
 (37)

The solution for $b_x(z, t)$ is (29)–(31) with D_m given by (37). Note that if $b_{xs}(t) = 0$ over the 24-h period, $D_m = 0$ for all m, and $b_x(z, t) = 0$ at all heights and times.

c. Solving for Π_x

In view of (29), b_x integrates to

$$\int_{z}^{\infty} b_{x}(z',t)dz' = e^{-\delta[t-\eta(t)]} \sum_{m=-\infty}^{\infty} \frac{D_{m}}{\sqrt{\sigma_{m}}} F_{m}(t)e^{-z\sqrt{\sigma_{m}}}.$$
 (38)

Applying (38) and (34) in (17) yields

$$\Pi_{x} = f \nu_{g} - e^{-\delta[t-\eta(t)]} \sum_{m=-\infty}^{\infty} \frac{D_{m} e^{-i\Phi_{m}/2}}{R_{m}^{1/2}} F_{m}(t) e^{-z\sqrt{\sigma_{m}}}.$$
 (39)

d. Solving for u_0 and v_0

Applying (38) in (18) yields

$$\frac{\partial \Gamma}{\partial t} = -if \Gamma + \nu(t) \frac{\partial^2 \Gamma}{\partial z^2} + e^{-\delta[t - \eta(t)]} \sum_{m = -\infty}^{\infty} \frac{D_m}{\sqrt{\sigma_m}} F_m(t) e^{-z\sqrt{\sigma_m}}.$$
(40)

To solve (40), we first seek its homogeneous solution, that is, the general solution Γ_h of

$$\frac{\partial \Gamma_h}{\partial t} = -if \,\Gamma_h + \nu(t) \frac{\partial^2 \Gamma_h}{\partial z^2}.\tag{41}$$

Separation of variables yields the solution of (41) as

$$\Gamma_h = \text{const} \times e^{\pm z\sqrt{\lambda}} e^{-ift + \lambda} \int_0^t \nu(t')dt', \tag{42}$$

where λ is a separation constant and the \pm symbol indicates that a sign choice must be made to ensure that $\Gamma_h \to 0$ as $z \to \infty$. In view of (42), the periodicity condition $\Gamma_h(z, 0) = \Gamma_h(z, t_{24})$ is satisfied by an infinite number of λ (one for each integer m) of the following form:

$$\lambda_m = i \left(\frac{f}{\overline{\nu}} + \frac{2m\pi}{\overline{\nu}t_{24}} \right). \tag{43}$$

The solution (42), generalized to include summation over m, is

$$\Gamma_h = e^{-if[t-\xi(t)]} \sum_{m=-\infty}^{\infty} G_m(t) E_m e^{-z\sqrt{\lambda_m}}, \tag{44}$$

$$G_m(t) \equiv e^{2m\pi i \, \xi(t)/t_{24}},$$
 (45)

$$\xi(t) \equiv \frac{1}{\overline{\nu}} \int_0^t \nu(t')dt',\tag{46}$$

where E_m are unknown constants. We have chosen the minus sign for the \pm symbol in (42) because, as will now show, $\Re(\sqrt{\lambda_m}) > 0$ for all m.

Setting $\lambda_m = r_m e^{i\varphi_m}$ in (43), yields $r_m \cos\varphi_m = 0$ and $r_m \sin\varphi_m = (2m\pi/t_{24} + f)/\overline{\nu}$, from which follow

$$r_m = \frac{\sqrt{(2m\pi/t_{24} + f)^2}}{\overline{\nu}} = \frac{|2m\pi/t_{24} + f|}{\overline{\nu}},$$
 (47)

 $\cos \varphi_{\rm m} = 0$, and $\sin \varphi_m = \operatorname{sgn}(2m\pi + ft_{24})(=1 \text{ for } 2m\pi + ft_{24} > 0; = -1 \text{ for } 2m\pi + ft_{24} < 0)$. We thus find that,

$$\varphi_m = \frac{\pi}{2} S_m,\tag{48}$$

where $S_m \equiv \text{sgn}(2m\pi + ft_{24})$, so

$$\sqrt{\lambda_m} = r_m^{1/2} e^{i\varphi_m/2} = r_m^{1/2} \left[\cos\left(\frac{\varphi_m}{2}\right) + i \sin\left(\frac{\varphi_m}{2}\right) \right]$$
$$= \frac{r_m^{1/2}}{\sqrt{2}} (1 + S_m i), \tag{49}$$

which shows that $\Re(\sqrt{\lambda_m}) > 0$ for all m.

We seek a particular solution Γ_p of (40) in the same form as the inhomogeneous term in that equation:

$$\Gamma_p = \sum_{m=-\infty}^{\infty} \frac{D_m}{\sqrt{\sigma_m}} H_m(t) e^{-z\sqrt{\sigma_m}},$$
(50)

where $H_m(t)$ is an unknown function. Applying (50) in (40) yields

$$\frac{dH_m}{dt} = \left[\sigma_m \nu(t) - if\right] H_m(t) + e^{-\delta \left[t - \eta(t)\right]} F_m(t). \tag{51}$$

Using the method of integrating factors, we solve (51) as

$$H_m(t) = e^{-ift + \sigma_m \overline{\nu} \, \xi(t)} [I_m(t) + Q_m], \tag{52}$$

where Q_m are unknown constants and $I_m(t) \equiv \int_0^t e^{\delta[\eta(t')-t']} e^{ift'-\sigma_m\overline{\nu}\xi(t')} F_m(t')dt'$, or

$$I_{m}(t) = \int_{0}^{t} e^{\delta \left[\eta(t') - \Pr \xi(t') - t' \right]} e^{i \left\{ f \, t' + 2m\pi \left[\eta(t') - \Pr \xi(t') \right] / t_{24} \right\}} dt', \quad (53)$$

where $\Pr \equiv \overline{\nu}/\overline{\kappa}$ is a Prandtl number. Since Γ_h is periodic, we need only impose the periodicity condition on Γ_p (via H_m) to ensure periodicity of the full solution. Setting $H_m(0) = H_m(t_{24})$ in (52) and using $\xi(t_{24}) = t_{24}$ yields $Q_m = e^{-if_{124} + \sigma_m \overline{\nu} t_{24}} [I_m(t_{24}) + Q_m]$, from which follows:

$$Q_{m} = -I_{m}(t_{24}) \left[\frac{1 - e^{-\Pr\delta t_{24}} e^{-i(f t_{24} - 2m\pi\Pr)}}{1 - 2e^{-\Pr\delta t_{24}} \cos(f t_{24} - 2m\pi\Pr) + e^{-2\Pr\delta t_{24}}} \right].$$
(54)

We obtain H_m as

$$H_{m}(t) = e^{\Pr\delta\xi(t)}e^{i[-f t + 2m\pi\Pr\xi(t)/t_{24}]} \times \left\{ I_{m}(t) - I_{m}(t_{24}) \left[\frac{1 - e^{-\Pr\delta t_{24}}e^{-i(f_{24} - 2m\pi\Pr)}}{1 - 2e^{-\Pr\delta t_{24}}\cos(f t_{24} - 2m\pi\Pr) + e^{-2\Pr\delta t_{24}}} \right] \right\}.$$
(55)

Affixing Γ_p to the homogeneous solution Γ_h yields the general solution of (40) as

$$\Gamma = \sum_{m=-\infty}^{\infty} \frac{e^{-i\Phi_m/2}}{R_m^{1/2}} D_m H_m(t) e^{-zR_m^{1/2} \left[\cos(\Phi_m/2) + i\sin(\Phi_m/2)\right]} + e^{-if[t-\xi(t)]} \sum_{m=-\infty}^{\infty} E_m G_m(t) e^{-zr_m^{1/2} (1+S_m i)/\sqrt{2}}.$$
(56)

To determine E_m , apply the no-slip condition (14) $[\Gamma(0, t) = -(u_g + iv_g)]$ in (56), and rearrange the result, obtaining

$$\sum_{m=-\infty}^{\infty} E_m G_m(t) = -e^{if[t-\xi(t)]} \left[u_g + i v_g + \sum_{m=-\infty}^{\infty} \frac{e^{-i\Phi_m/2}}{R_m^{1/2}} D_m H_m(t) \right].$$
(57)

Multiplying (57) by $\nu(t)G_n^*(t)$, and integrating the resulting equation over 24 h using

$$\int_{0}^{t_{24}} \nu(t') G_m(t') G_n^*(t') dt' = \delta_{mn} t_{24} \overline{\nu}, \tag{58}$$

[the proof of which is virtually the same as that leading to (36)] then yields:

$$E_{m} = -\frac{1}{t_{24}\overline{\nu}} \int_{0}^{t_{24}} \nu(t') e^{i\{f[t'-\xi(t')]-2m\pi\xi(t')\}/t_{24}}$$

$$\times \left[u_{g} + i v_{g} + \sum_{q=-\infty}^{\infty} \frac{e^{-i\Phi_{q}/2}}{R_{q}^{1/2}} D_{q} H_{q}(t') \right] dt'. \quad (59)$$

e. Comment on the composite problem

It can be shown that the ageostrophic wind solution (56) with D_m given by (37) and E_m given by (59) can be partitioned into the sum of the solution of a free-atmosphere-PGF (free-atmosphere geostrophic wind)-forced problem, and the solution of a surface-buoyancy-gradient-forced problem. In other words, the solution of the composite problem, where both forcings are operating, is the sum of the solutions associated with the individual forcings. Accordingly, if the times and heights of a local wind extremum in the two individually forced problems are similar, the magnitude of that extremum in the composite solution is similar to the sum of the magnitudes of the extrema in the individually forced problems.

4. Reference run and sensitivity experiments

The solutions were evaluated over 24 h starting from sunrise (t = 0 s) with 10 001 terms retained in each series, and the integrals approximated using the trapezoidal formula with a time step of $\Delta t = 4.32$ s (20 001 computational times). Results were output with a vertical grid spacing of $\Delta z = 20$ m. The wind speeds, heights, and times of features in the analytical solution are expressed to the nearest 0.1 m s⁻¹, 20 m, and 0.1 h, respectively.

The mixing coefficients v(t) and $\kappa(t)$ were slightly modified step functions that decreased rapidly at sunset $(t = t_{\text{set}})$ from large daytime values of v_d and κ_d to small nighttime values of v_n and κ_n , and increased rapidly back to daytime values at sunrise. These changes occurred as linear-in-time variations over very short (3 min) intervals.³ The values chosen for v_d , κ_d , v_n , and κ_n were informed by estimates of v and κ (or v and v and v from laboratory and atmospheric measurements in statically stable (relevant to nighttime) and unstable (relevant to daytime) environments. Under unstable conditions, v is typically in a 10–100 m² s⁻¹ range (Yamada and Mellor 1975; Tombrou et al. 2007; Dandou et al. 2009), and κ is less than v (Pr < 1), with Pr as low as 0.3 in very unstable regimes

 $^{^3}$ Use of these intervals reduced the number of terms in the Fourier series needed to accurately represent the winds. The computed surface values of u and v at any time in any of our experiments differed from 0 m s $^{-1}$ (no-slip condition) by no more than $0.08 \, \mathrm{m \ s}^{-1}$.

TABLE 1. Parameter settings for reference experiment REF. Time of sunset (t_{sef}) is in hours after sunrise.

Parameter	Value			
f	$8.6 \times 10^{-5} \text{ s}^{-1} \text{ (lat } \approx 36.4^{\circ}\text{N)}$			
b_{xs}	$-2 \times 10^{-7} \mathrm{s}^{-2}$			
$t_{ m set}$	12 h			
ν_d , κ_d	$50 \text{ m}^2 \text{ s}^{-1}$			
ν_n, κ_n	$1 \text{ m}^2 \text{ s}^{-1}$			
u_g	0 m s^{-1}			
0	$10~\mathrm{m~s^{-1}}$			
$v_g \ \delta$	$0.2 \mathrm{day}^{-1}$			

(Businger et al. 1971; Gibson and Launder 1978; Ueda et al. 1981). In stable conditions, ν is typically in a 0.01–1 m² s⁻¹ range (Sharan and Gopalakrishnan 1997; Mahrt and Vickers 2005; Dandou et al. 2009), while Pr varies from ~1 to over 100 (Ueda et al. 1981; Howell and Sun 1999; Kurbatskiy and Kurbatskaya 2011; Kitamura et al. 2013).

a. Reference run

A reference experiment (REF) was conducted in which the free-atmosphere geostrophic wind was southerly at 10 m s⁻¹, and the surface buoyancy decreased eastward at a rate of -0.2 m s⁻² (1000 km)⁻¹ [virtual potential temperature decreased eastward at a rate of -6 K (1000 km)⁻¹], that is, $b_{xs} = -2 \times 10^{-7}$ s⁻² (independent of time). Associated with this buoyancy gradient was a northerly thermal wind. The free-atmosphere PGF and the PGF associated with the

buoyancy gradient both pointed westward and contributed to a southerly low-level geostrophic wind. The mixing coefficients decreased at sunset ($t_{\rm set} = 12 \, \rm h$) from daytime values of $v_d = \kappa_d = 50 \, \rm m^2 \, s^{-1}$ to nighttime values of $v_n = \kappa_n = 1 \, \rm m^2 \, s^{-1}$. The Coriolis parameter was set to $f = 8.6 \times 10^{-5} \, \rm s^{-1}$ (latitude $\approx 36.4^{\circ} \rm N$). As in Egger (1985) and S16, the radiative damping time scale was set at 5 days ($\delta = 0.2 \, \rm day^{-1}$). The parameter values in REF (Table 1) are also the default values in the southerly jet sensitivity experiments (Table 2).

Time-height plots of the winds in REF are shown in Fig. 1. During much of the afternoon, the low-level v was subgeostrophic, and the low-level u was negative (easterly) with a peak of about -8 m s⁻¹. This easterly flow component was directed across isobars toward low pressure. The easterly and southerly flow components intensified rapidly after sunset, especially at low levels. The southerly wind peaked at $v_{\text{max}} = 27.4$ m s⁻¹ at time $t_{\text{umin}} = 20.7$ h at height $z_{\text{umax}} = 420$ m. The easterly wind peaked at $u_{\text{min}} = -13.2$ m s⁻¹ at time $t_{\text{umin}} = 16.2$ h at height $z_{\text{umin}} = 240$ m. Additionally, after sunset, a zone of westerly flow on top of the low-level easterly flow descended and intensified. The intensification ended abruptly at sunrise, with the westerly wind peaking at $v_{\text{max}} = 8.7$ m s⁻¹ at height $v_{\text{umax}} = 640$ m. The results are summarized in Table 3.

To compare the time of the wind speed maximum in REF with that predicted from the inviscid IO theory, we constructed a circular IO hodograph (not shown) that was (i) centered on the free-atmosphere geostrophic wind and (ii) passed through the model-predicted wind at sunset at the height at which the peak wind speed eventually occurred.

TABLE 2. Southerly low-level jet experiments. The parameter values in each experiment are as in REF (Table 1) except as noted in the description.

Expt	Description
REF	Reference experiment
WEAKBX	Weak surface buoyancy gradient: $b_{xs} = -1 \times 10^{-7} \text{ s}^{-2}$
STRONGBX	Strong surface buoyancy gradient: $b_{xs} = -3 \times 10^{-7} \text{ s}^{-2}$
NOBX	No surface buoyancy gradient: $b_{xs} = 0 \text{ s}^{-2}$
$NOBX\nu_d^-$	As in NOBX, but with daytime ν reduced to 20 m ² s ⁻¹
$NOBX\nu_d^+$	As in NOBX, but with daytime ν increased to 100 m ² s ⁻¹
NONIGHTBX	No surface buoyancy gradient at night: $b_{xs} = 0 \text{ s}^{-2}$ for $t > t_{\text{set}}$
REVNIGHTBX	Reversed surface buoyancy gradient at night: $b_{xs} = 2 \times 10^{-7} \text{ s}^{-2}$ for $t > t_{\text{set}}$
NOGEOS	No free-atmosphere geostrophic wind: u_g , $v_g = (0, 0)$ m s ⁻¹
$NOGEOS \nu_d^- \kappa_d^-$	As in NOGEOS, but with daytime ν and κ reduced to 20 m ² s ⁻¹
$NOGEOS \nu_d^+ \kappa_d^+$	As in NOGEOS, but with daytime ν and κ increased to 100 m ² s ⁻¹
$NOGEOSv_d^-$	As in NOGEOS, but with daytime ν reduced to 20 m ² s ⁻¹
$NOGEOSv_d^+$	As in NOGEOS, but with daytime ν increased to 100 m ² s ⁻¹
$NOGEOS\kappa_d^-$	As in NOGEOS, but with daytime κ reduced to 20 m ² s ⁻¹
$NOGEOS\kappa_d^+$	As in NOGEOS, but with daytime κ increased to 100 m ² s ⁻¹
$NOGEOS \nu_n^- \kappa_n^-$	As in NOGEOS, but with nighttime ν and κ reduced to 0.2 m ² s ⁻¹
$NOGEOS\nu_n^+\kappa_n^+$	As in NOGEOS, but with nighttime ν and κ increased to 5 m ² s ⁻¹
$NOGEOS\nu_n^-$	As in NOGEOS, but with nighttime ν reduced to 0.2 m ² s ⁻¹
$NOGEOS\nu_n^+$	As in NOGEOS, but with nighttime ν increased to 5 m ² s ⁻¹
$NOGEOS\kappa_n^-$	As in NOGEOS, but with nighttime κ reduced to 0.2 m ² s ⁻¹
$NOGEOS\kappa_n^+$	As in NOGEOS, but with nighttime κ increased to 5 m ² s ⁻¹
CORf	$f = 7.3 \times 10^{-5} \text{ s}^{-1} \text{ (lat } \approx 30^{\circ} \text{N)}$
$CORf^+$	$f = 9.7 \times 10^{-5} \text{ s}^{-1} \text{ (lat } \approx 42^{\circ}\text{N)}$
$\mathrm{DAMP}\delta^-$	$\delta = 0.1 \text{ day}^{-1} \text{ (10-day radiative damping time scale)}$
$DAMP\delta^+$	$\delta = 1 \text{ day}^{-1} \text{ (1-day radiative damping time scale)}$

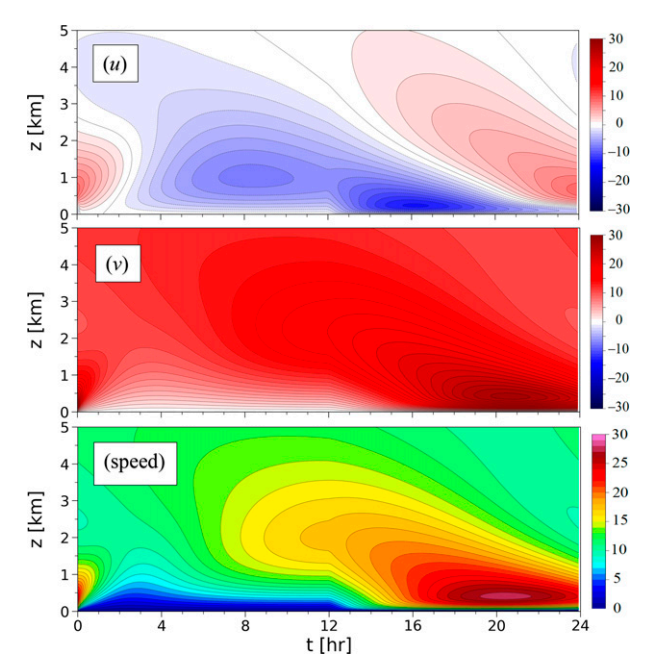


FIG. 1. Time-height plots of (top) u (m s⁻¹), (middle) v (m s⁻¹), and (bottom) wind speed (m s⁻¹) in REF, a reference experiment in which the flow is forced by a surface buoyancy gradient of $b_{xs} = -2 \times 10^{-7} \text{ s}^{-2}$ and a southerly free-atmosphere geostrophic wind ($u_g = 0 \text{ m s}^{-1}$, $v_g = 10 \text{ m s}^{-1}$). Time (t) is in hours after sunrise. Sunset is at t = 12 h. See Table 1 for all parameter values.

That hodograph showed that a parcel in an inviscid IO launched at sunset with wind components from the analytical model would attain its peak speed after traversing about 75% of half of the IO circle. The inviscid theory would therefore predict the time to the speed maximum to be about 75% of half of the inertial period, that is, $0.75 \times 0.5 \times 2\pi/f = \sim 7.6 \text{ h}$ after sunset, or ~19.6 h after sunrise. This was about 1 h earlier than the model prediction of ~20.7 h. Additional experiments (not shown) explored the sensitivity of the time of the peak speed to the mixing coefficients. When ν_d and κ_d were reduced to $20 \text{ m}^2 \text{ s}^{-1}$, the wind speed peaked only $\sim 0.5 \text{ h}$ later than in the inviscid theory. However, when κ_d alone was reduced, the time of the speed maximum hardly changed. Similar experiments with the nighttime mixing coefficients showed that the time of the speed maximum decreased when ν_n increased (opposite to the trend seen with ν_d) but was relatively insensitive to κ_n . We conclude that the time of the speed maximum in REF is qualitatively similar to that predicted by the inviscid theory, with differences that arise, in large part, from the mixing of momentum.

b. Southerly low-level jet experiments

Experiments (Table 2) were conducted to explore model sensitivities in REF-like cases where the PGF forcings—the free-atmosphere PGF and/or the PGF arising from the buoyancy gradient—pointed westward (southerly geostrophic wind). In these runs, the model predicted that a southerly

wind component would dominate, with v being positive above the ground. Results from these experiments are summarized in Table 3.

NOBX and NOGEOS were run to see how much of the flow in REF was driven by the free-atmosphere PGF (freeatmosphere geostrophic wind) versus the PGF associated with the buoyancy gradient. There was no surface buoyancy gradient $(b_{xs} = 0 \text{ s}^{-2})$ in NOBX [so $b_x(z, t) = 0$ for all z and t; see discussion of (37)], and no free-atmosphere geostrophic wind $(u_g = v_g = 0 \text{ m s}^{-1})$ in NOGEOS. From Figs. 2 and 3 and Table 3 we see that the spatial and temporal patterns of the wind components, including the times and heights of the extrema, are similar to those in REF, but with amplitudes reduced by ~40% in NOBX and by ~60% in NOGEOS. Consistent with the composition principle of section 3e, the v_{max} in REF is close to the sum of the v_{max} from NOBX and NOGEOS, while the u_{max} (and u_{min}) in REF are close to the corresponding sums of u_{max} (and u_{min}) from NOBX and NOGEOS.

Additional REF-like runs were made with a surface buoyancy gradient that was 50% weaker than in REF ($b_{xs} = -1 \times 10^{-7} \text{ s}^{-2}$ in WEAKBX) and 50% stronger than in REF ($b_{xs} = -3 \times 10^{-7} \text{ s}^{-2}$ in STRONGBX); these yielded peak southerly, easterly, and westerly winds that were ~20% weaker and ~20% stronger, respectively, than the corresponding components in REF, with little change in the times or heights of the extrema

Further experiments of NOBX- and NOGEOS-type examined the sensitivity of purely free-atmosphere-PGF-forced and purely surface-buoyancy-gradient-forced flows to the eddy mixing coefficients. Experiment NOBX⁴ was rerun with the daytime eddy viscosity decreased to $\nu_d = 20~\text{m}^2~\text{s}^{-1}$ in NOBX ν_d^- , and increased to $\nu_d = 100~\text{m}^2~\text{s}^{-1}$ in NOBX ν_d^+ . Since ν_n was not changed, there was a greater decrease in eddy viscosity from day to night in NOBX ν_d^+ than in NOBX ν_d^- and, consistent with the B57 premise of a turbulence-shutdown-induced IO, the Shapiro and Fedorovich (2010) theory, and S16, the peak winds were larger in the run with the larger decrease of turbulence at sunset (NOBX ν_d^+). However, the effect of the larger decrease was modest, with $\nu_{\rm max}$ in NOBX ν_d^+ exceeding that in NOBX ν_d^- by only $2.1~\text{m}~\text{s}^{-1}$.

Unlike the NOBX-like flows, the NOGEOS-like flows varied with κ as well as ν . The daytime values of ν and κ were reduced to $20~\text{m}^2~\text{s}^{-1}$ in NOGEOS $\nu_d^-\kappa_d^-$, and increased to $100~\text{m}^2~\text{s}^{-1}$ in NOGEOS $\nu_d^+\kappa_d^+$. Compared to a NOGEOS ν_{max} of $11.5~\text{m}~\text{s}^{-1}$, ν_{max} was $6.5~\text{m}~\text{s}^{-1}$ in NOGEOS $\nu_d^-\kappa_d^-$ and $17.3~\text{m}~\text{s}^{-1}$ in NOGEOS $\nu_d^+\kappa_d^+$. To see whether these differences in ν_{max} were due more to changes in one coefficient than the other, we ran experiments in which only ν_d was changed ($20~\text{m}^2~\text{s}^{-1}$ in NOGEOS ν_d^+ ; $100~\text{m}^2~\text{s}^{-1}$ in NOGEOS ν_d^+), and only κ_d was changed ($20~\text{m}^2~\text{s}^{-1}$ in NOGEOS ν_d^+), and only κ_d was changed ($20~\text{m}^2~\text{s}^{-1}$ in

⁴ Theoretically, κ has no influence on NOBX-type flows; all values of κ should yield the same solution. However, setting $\kappa = 0$ m² s⁻¹ does yield computational singularities (0/0). These can be avoided by setting κ to a small but non-zero value.

TABLE 3. Characteristics of winds in the southerly NLLJ experiments. Local maxima of u and v (u_{max} and v_{max}) occurred at heights z_{umax} and z_{umax} and at times t_{umax} and t_{umax} , respectively. The local minimum of u ($u_{min} < 0$) occurred at height z_{umin} and at time t_{umin} . There was no local minimum of v. Winds, heights, and times are given to the nearest 0.1 m s⁻¹, 20 m, and 0.1 h, respectively. In these experiments, the peak wind speed (not given) was only slightly larger than v_{max} ; the largest difference between the peak speed and v_{max} in any experiment barely exceeded 1 m s⁻¹.

Expt	$v_{max} \ (m \ s^{-1})$	z_{vmax} (m)	t_{vmax} (h)	$u_{\text{max}} \text{ (m s}^{-1})$	z _{umax} (m)	t _{umax} (h)	$u_{\min} (\text{m s}^{-1})$	z _{umin} (m)	t _{umin} (h)
REF	27.4	420	20.7	8.7	640	0.0	-13.2	240	16.2
WEAKBX	21.7	420	20.7	6.7	640	0.0	-10.3	240	16.2
STRONGBX	33.1	400	20.7	10.6	640	0.0	-16.1	240	16.2
NOBX	16.0	440	20.7	4.7	640	0.0	-7.4	240	16.2
$\mathrm{NOBX} u_d^-$	14.7	400	20.0	3.7	580	0.0	-6.6	200	15.9
$NOBX\nu_d^+$	16.8	460	21.1	5.2	700	0.0	-8.0	260	16.4
NONIGHTBX	27.2	420	20.7	8.6	640	0.0	-13.1	240	16.2
REVNIGHTBX	27.0	420	20.6	8.6	640	0.0	-13.0	240	16.1
NOGEOS	11.5	400	20.6	4.0	640	0.0	-5.8	240	16.1
$NOGEOS \nu_d^- \kappa_d^-$	6.5	360	20.0	2.0	560	0.0	-3.3	200	15.8
NOGEOS $\nu_d^+ \kappa_d^+$	17.3	420	21.0	6.2	700	0.0	-8.7	260	16.3
$NOGEOS\nu_d^-$	10.6	380	19.8	3.2	560	0.0	-5.1	200	15.7
$NOGEOS\nu_d^+$	12.0	420	21.0	4.2	680	0.0	-6.2	260	16.4
$NOGEOS\kappa_d^-$	7.0	380	20.7	2.4	620	0.0	-3.7	220	16.2
$NOGEOS\kappa_d^+$	16.5	400	20.6	5.7	640	0.0	-8.2	240	16.1
NOGEOS $\nu_n^- \kappa_n^-$	13.1	200	21.3	4.7	360	0.0	-6.6	120	16.6
NOGEOS $\nu_n^+ \kappa_n^+$	9.4	740	19.4	2.4	1220	23.4	-4.7	400	15.4
$NOGEOS\nu_n^-$	13.2	200	21.3	4.7	360	0.0	-6.7	120	16.6
$NOGEOS\nu_n^+$	9.0	740	19.3	2.4	1220	23.4	-4.5	400	15.4
$NOGEOS\kappa_n^-$	11.4	400	20.6	3.9	640	0.0	-5.7	240	16.1
$NOGEOS\kappa_n^+$	11.9	400	20.6	4.1	640	0.0	-6.0	240	16.1
CORf	30.6	480	21.8	11.1	1520	0.0	-14.8	280	16.6
$CORf^+$	26.2	380	19.8	8.7	540	0.0	-12.6	220	15.8
$\text{DAMP}\delta^-$	32.5	420	20.7	10.1	640	0.0	-15.6	240	16.2
$DAMP\delta^+$	20.5	420	20.5	6.9	620	0.0	-10.0	240	16.1

 $NOGEOS\kappa_d^-$; 100 m² s⁻¹ in $NOGEOS\kappa_d^+$). The v_{max} in $NOGEOS\nu_d^+$ (12.0 m s⁻¹) and $NOGEOS\nu_d^-$ (10.6 m s⁻¹) differed from that in NOGEOS (11.5 m s⁻¹) by less than 1 m s⁻¹, while the v_{max} in NOGEOS κ_d^+ (16.5 m s⁻¹) and NOGEOS κ_d^- (7.0 m s⁻¹) differed from that in NOGEOS by about 5 m s⁻¹. Moreover, the v_{max} in NOGEOS κ_d^+ and NOGEOS κ_d^- were very close to the values in NOGEOS $\nu_d^+ \kappa_d^+$ and NOGEOS $\nu_d^- \kappa_d^-$, respectively. Thus, model jet strength was impacted more by changes in the daytime mixing of heat (via κ_d) than changes in the daytime mixing of momentum (via ν_d). The strong sensitivity to κ_d arises from the fact that a large κ_d supports a large upward extension of surface-based thermal perturbations and a stronger low-level southerly geostrophic wind [from (17)], which would promote a stronger IO-like response. We remind the reader, however, that these sensitivities pertain to experiments in which there was no free-atmosphere geostrophic wind.

Interestingly, the sensitivity of NOGEOS flows to the mixing coefficients was reversed at night. When ν_n and κ_n were reduced to 0.2 m² s⁻¹ (NOGEOS $\nu_n^-\kappa_n^-$), $\nu_{\rm max}$ increased to 13.1 m s⁻¹, and when ν_n and κ_n were increased to 5 m² s⁻¹ (NOGEOS $\nu_n^+\kappa_n^+$), $\nu_{\rm max}$ decreased to 9.4 m s⁻¹. Additional tests showed that these changes were mostly due to changes in ν_n : decreasing κ_n alone to 0.2 m² s⁻¹ (NOGEOS κ_n^-) or increasing κ_n alone to 5 m² s⁻¹ (NOGEOS κ_n^+) yielded similar $\nu_{\rm max}$ values (11.4 and 11.9 m s⁻¹, respectively). In contrast,

decreasing ν_n alone to 0.2 m² s⁻¹ (NOGEOS ν_n^-) and increasing ν_n alone to 5 m² s⁻¹ (NOGEOS ν_n^+) yielded $\nu_{\rm max}$ values of 13.2 and 9.0 m s⁻¹, respectively. Obtaining stronger jet winds with larger decreases of eddy viscosity from day to night (as in NOGEOS ν_n^-) is consistent with the IO mechanism.

The insensitivity of the NOGEOS-type flows to changes in the nighttime eddy diffusivity suggests that the nighttime surface buoyancy gradient may have little direct impact on the NLLJ. This hypothesis was supported by results from an experiment in which $b_{xs}(t)$ was set to zero at night (NONIGHTBX), and an experiment in which $b_{xs}(t)$ at night was reversed from its daytime value (REVNIGHTBX). Although these day-to-night time dependences were extreme, the flows in both runs differed insignificantly from that in REF, with the v_{max} in NONIGHTBX (27.2 m s⁻¹) and REVNIGHTBX (27.0 m s⁻¹) being weaker than that in REF by only 0.2 and 0.4 m s⁻¹, respectively. These results suggest that the turbulent mixing of heat at night is too weak (κ_n too small) to effectively spread the nocturnal surface thermal gradient into the vertical.

The sensitivity of the southerly jets to the Coriolis parameter was examined in $CORf^+$ ($f = 9.7 \times 10^{-5} \text{ s}^{-1}$; latitude $\approx 42^{\circ}\text{N}$) and $CORf^-$ ($f = 7.3 \times 10^{-5} \text{ s}^{-1}$; latitude $\approx 30^{\circ}\text{N}$). In proceeding from the higher to lower latitudes, v_{max} increased by about 4.4 m s^{-1} or 16% of the v_{max} in REF. In contrast, the increase in v_{max} across that same latitude band in S16

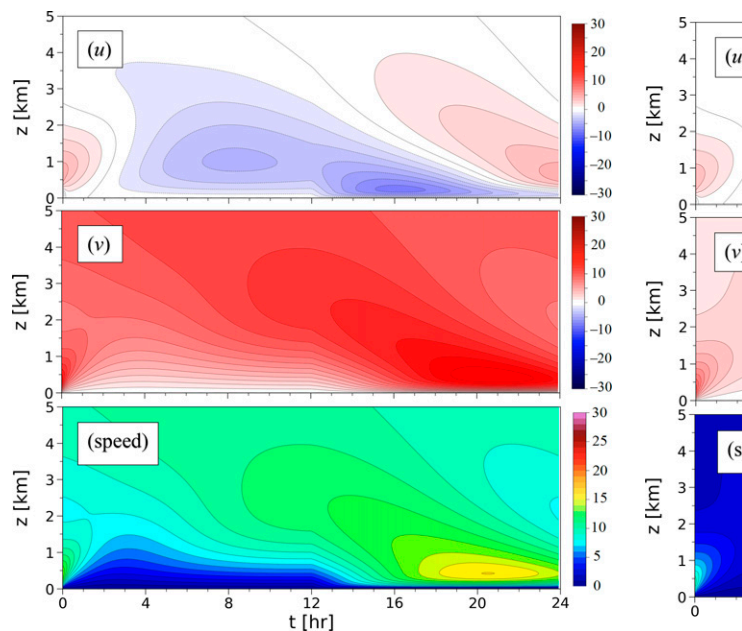


FIG. 2. Time–height plots of (top) u (m s⁻¹), (middle) v (m s⁻¹), and (bottom) wind speed (m s⁻¹) in NOBX, an experiment in which a barotropic flow ($b_{xs} = 0 \text{ s}^{-2}$) is forced by a southerly free-atmosphere geostrophic wind ($u_g = 0 \text{ m s}^{-1}$, $v_g = 10 \text{ m s}^{-1}$). Time (t) is in hours after sunrise. Sunset is at t = 12 h. See Table 1 for all parameter values.

(recalling that baroclinicity in \$16 was associated with a uniformly heated slope) was only 0.9 m s⁻¹, or 4% of the peak in that study's reference run (cf. v_{max} in BH f^+ and BH f^- to that in BH in \$16 Table 3). Although the 16% increase with decreasing latitude seen in the present study may be considered relatively minor, the increase is 4 times larger than in S16, where there were no along-slope buoyancy variations. Consistent with the longer inertial period in CORf⁻, the southerly wind in $CORf^-$ peaks 2 h later than in $CORf^+$. Additionally, the descent and intensification of the westerly winds during the latter part of the night are delayed in CORf-. Since the westerly wind intensification is "arrested" by the mixing attending the morning transition, the height of the westerly wind maximum at its most intense (sunrise) is larger in $CORf^-$ ($z_{umax} = 1520 \text{ m}$) than in $CORf^+$ ($z_{umax} = 540 \text{ m}$).

Last, we examined model sensitivity to radiative damping. In DAMP δ^+ , where δ was increased to $(1 \text{ day})^{-1}$, v_{max} decreased to 20.5 m s^{-1} , while in DAMP δ^- , where δ was decreased to $(10 \text{ days})^{-1}$, v_{max} increased to 32.5 m s^{-1} . The ~25% increase in v_{max} in DAMP δ^- (compared to v_{max} in REF) and ~20% decrease in v_{max} in DAMP δ^+ were matched by similar relative increases/decreases in u_{max} and u_{min} . In contrast, the changes in v_{max} seen in S16 with the same damping parameters (cf. BH δ^+ and BH δ^- in Table 3 of S16) were much smaller (<4%), and led to the conclusion there that the flow was not very sensitive to δ . The larger sensitivity in the present model may be due to the fact that one of the processes in S16—adiabatic warming/cooling associated

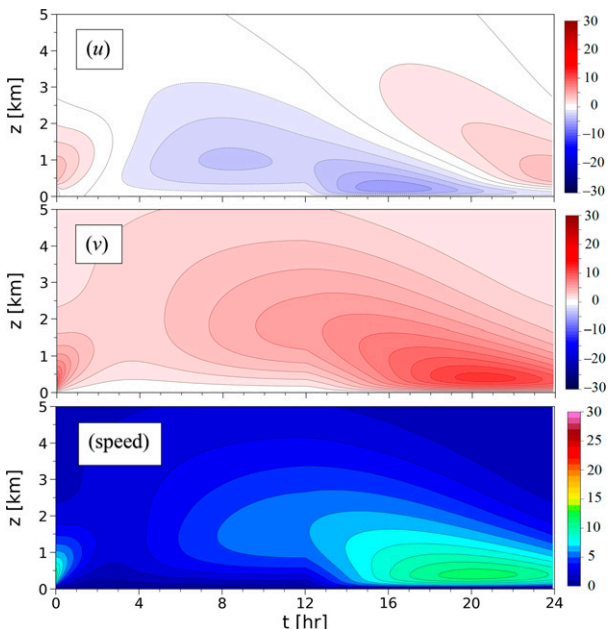


FIG. 3. Time–height plots of (top) u (m s⁻¹), (middle) v (m s⁻¹), and (bottom) wind speed (m s⁻¹) in NOGEOS, an experiment in which the flow is forced by a surface buoyancy gradient ($b_{xs} = -2 \times 10^{-7} \text{ s}^{-2}$) without a free-atmosphere geostrophic wind ($u_g = 0 \text{ m s}^{-1}$, $v_g = 0 \text{ m s}^{-1}$). Time (t) is in hours after sunrise. Sunset is at t = 12 h. See Table 1 for all parameter values.

with downslope/upslope motions—does not operate in our flat-terrain model. With one less forcing term in the thermal energy equation, the remaining terms, including the radiative damping term, assume more important roles.

c. Free-atmospheric geostrophic winds in other directions

Additional experiments were run for free-atmosphere geostrophic winds that had the same magnitude as in REF (10 m s⁻¹), but were northerly (GEOS-N), westerly (GEOS-W), or easterly (GEOS-E). The corresponding free-atmosphere PGFs pointed eastward (GEOS-N), northward (GEOS-W), and southward (GEOS-E). In contrast to the free-atmosphere PGF in REF, which acted in the same direction as the PGF associated with the buoyancy gradient, the free-atmosphere PGF in GEOS-N opposed the PGF associated with the buoyancy gradient (yielding a PGF weaker than in REF), and the free-atmosphere PGFs in GEOS-W and GEOS-E were perpendicular to the PGF associated with the buoyancy gradient. Time-height plots of the winds in these experiments are shown in Figs. 4-6. Not surprisingly, the winds in GEOS-N (Fig. 4) were much weaker than in REF, and there was not even a local maximum in v or the wind speed. The peak speeds in GEOS-W (Fig. 5) and GEOS-E (Fig. 6) were similar (just exceeding 20 m s⁻¹) but, unlike REF, were attained with comparable contributions by u and v. The speed maximum occurred about halfway between the times u and v attained their peak values. The u fields in GEOS-W and GEOS-E were quite different (as were the v

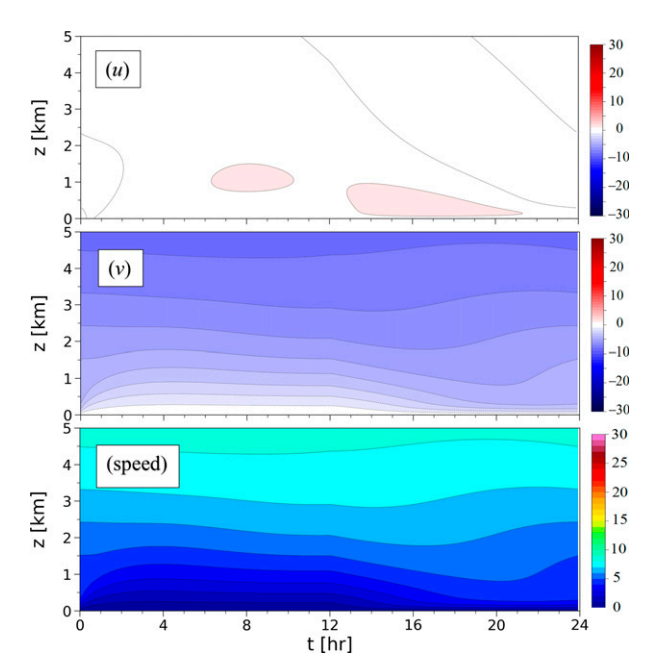


FIG. 4. Time–height plots of (top) u (m s⁻¹), (middle) v (m s⁻¹), and (bottom) wind speed (m s⁻¹) in GEOS-N, an experiment in which the flow is forced by a surface buoyancy gradient of $b_{xs} = -2 \times 10^{-7} \text{ s}^{-2}$ and a northerly free-atmosphere geostrophic wind ($u_g = 0 \text{ m s}^{-1}$, $v_g = -10 \text{ m s}^{-1}$). Time (t) is in hours after sunrise. Sunset is at t = 12 h. See Table 1 for all parameter values.

fields), but a coordinate rotation through 90° brings u and v from GEOS-E into closer agreement with u and v from GEOS-W.

5. A baroclinic NLLJ over the Great Plains on 1 May 2020

The analytical model was applied to a baroclinic NLLJ that developed over the Great Plains during the early morning hours of 1 May 2020. The model winds were compared to Doppler lidar winds from the ARM SGP central facility near Lamont, Oklahoma, a location that is within the baroclinic zone, has a very weak slope (there is no slope in the model), and is well east of a trough evident in surface analyses (not shown) that could have affected the wind and thermal fields in western Kansas and the western parts of the Texas and Oklahoma Panhandles. The 1200 UTC (near time of sunrise at Lamont) soundings from the NWS Radiosonde Network showed that a strong southerly wind-dominated NLLJ (peak winds varied from south-southeasterly to west-southwesterly) extended from southern Texas through northern South Dakota (Table 4). During the previous afternoon, a largeamplitude ridge-trough pattern brought northwesterly winds at 500 hPa over much of this region (Fig. 7a). It is

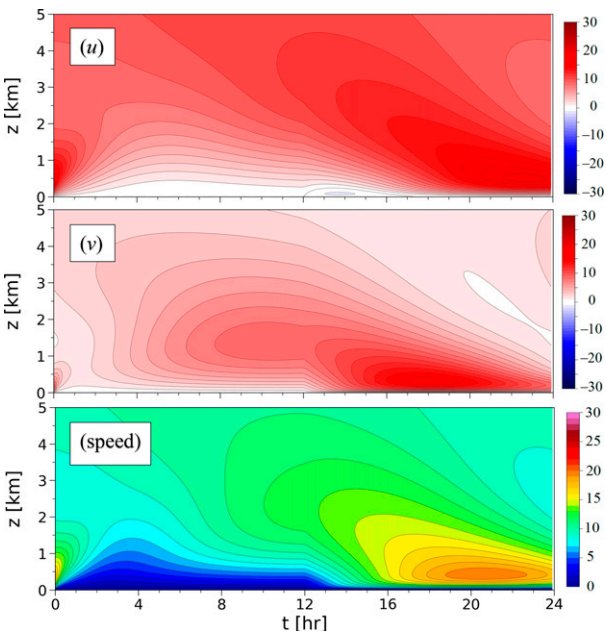


FIG. 5. Time—height plots of (top) u (m s⁻¹), (middle) v (m s⁻¹), and (bottom) wind speed (m s⁻¹) in GEOS-W, an experiment in which the flow is forced by a surface buoyancy gradient of $b_{xs} = -2 \times 10^{-7} \text{ s}^{-2}$ and a westerly free-atmosphere geostrophic wind ($u_g = 10 \text{ m s}^{-1}$, $v_g = 0 \text{ m s}^{-1}$). Time (t) is in hours after sunrise. Sunset is at t = 12 h. See Table 1 for all parameter values.

perhaps unexpected that a strong NLLJ could develop in the presence of free-atmosphere winds with a northerly component, but the low-level (850 hPa) thermal forcing was extensive (Fig. 7b) and supported a strong southerly low-level geostrophic wind. The ERA5 (Hersbach et al. 2020) surface analysis for 2200 UTC 30 April 2020 (Fig. 8a) showed a fairly uniform primarily westward-directed thermal gradient extending over Oklahoma. The 1000 UTC 1 May 2020 ERA5 surface analysis (Fig. 8b) showed that despite the cooling that had taken place during the night, the strength of the thermal gradient over the state (excluding the panhandle) was largely preserved. A vertical cross section (Fig. 9) of ERA5 winds and θ_v at 2200 UTC 30 April 2020 along latitude = 36.5°N (near Lamont) showed a westward increase in the depth of a well-mixed dry convective boundary layer.

Time-height plots of Doppler lidar winds from the ARM SGP central facility (ARM 2010) showed the development of a strong NLLJ (Fig. 10), with a peak speed of 29 m s⁻¹ attained at height 600 m (all heights expressed AGL) at 1015 UTC 1 May 2020, with a secondary peak of 28 m s⁻¹ reached 1.5 h later at a height of 700 m. The first speed maximum occurred at roughly the same height and time as the peak v component (which was 25 m s⁻¹), while the second speed maximum occurred at roughly the same height and time as the peak u component (which was 20 m s⁻¹). The low-level velocity vectors (e.g., at z = 500 m) turned

⁵ The above-noted trough may have affected the jets over Amarillo and Dodge City, which were more westerly than the jets over the other stations.

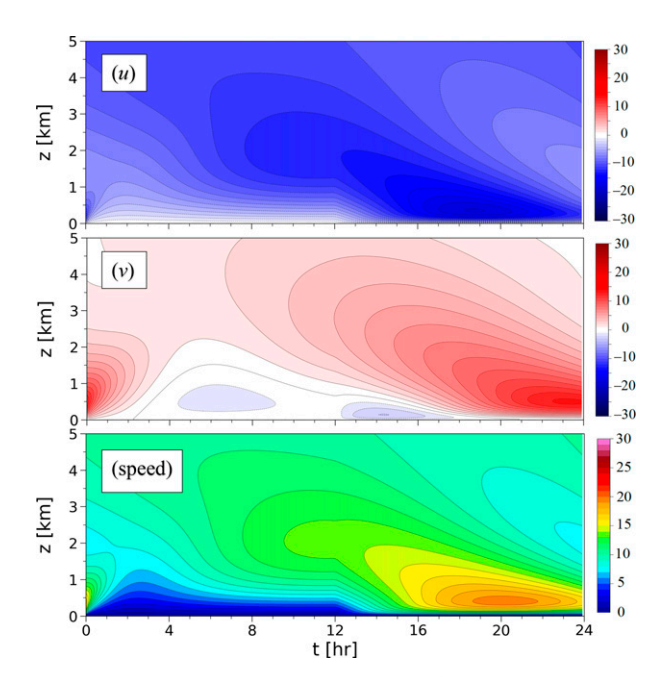


FIG. 6. Time-height plots of (top) u (m s⁻¹), (middle) v (m s⁻¹), and (bottom) wind speed (m s⁻¹) in GEOS-E, an experiment in which the flow is forced by a surface buoyancy gradient of $b_{xs} = -2 \times 10^{-7}$ s⁻² and an easterly free-atmosphere geostrophic wind ($u_g = -10$ m s⁻¹, $v_g = 0$ m s⁻¹). Time (t) is in hours after sunrise. Sunset is at t = 12 h. See Table 1 for all parameter values.

anticyclonically through the night, as in an IO. We note a tendency for the heights of the maximum v-wind and wind speed to increase with time from ~ 0300 UTC (about 2 h after sunset) through most of the rest of the night.

A vertical cross section of ERA5 winds and θ_v at 1000 UTC 1 May 2020, near the time of peak speed in the lidar data, showed NLLJ winds were widespread over 6° of longitude straddling Lamont (Fig. 11). At this time, the ERA5 winds over Lamont were in close agreement with the lidar winds, with a peak v of 22 m s⁻¹ (25 m s⁻¹ in lidar data), and a peak u of 15 m s⁻¹ (17 m s⁻¹ in lidar data). A weak easterly flow near the surface was present in ERA5 output ($u \approx -1$ m s⁻¹) and lidar data ($u \approx -4$ m s⁻¹).

ERA5 wind and θ_v analyses near Lamont at 2200 UTC 30 April 2020 were used to calculate the free-atmosphere geostrophic winds and surface buoyancy gradient for the analytical model. The surface buoyancy gradient was obtained from $b_{xs} = [g/\Theta(0)] \ \partial \theta_v \partial x - N^2 \partial z_T \partial x \ [\Theta(0) = 300 \text{ K}, N = 0.01 \text{ s}^{-1}, z_T \text{ is terrain height}]. With the slope at Lamont estimated as <math>\partial z_T / \partial x = -0.0012 \text{ rad} \ (-0.068^\circ)$ and $\partial \theta_v / \partial x$ estimated as $-2.36 \times 10^{-5} \text{ K m}^{-1} \ [\text{using ERA5} \ \theta_v \ data \ (\text{Fig. 8}) \ \text{from } 100 \text{ km}$ east and west of Lamont], we get $b_{xs} = -7.7 \times 10^{-7} \text{ s}^{-2} + 1.2 \times 10^{-7} \text{ s}^{-2} = -6.5 \times 10^{-7} \text{ s}^{-2} \ (\text{note relative smallness of slope term, the second term on the left-hand side). The free-atmosphere geostrophic wind components were estimated from Fig. 9, under the assumption that the free-atmosphere flow was geostrophic and barotropic. Unfortunately, estimating$

TABLE 4. Peak wind speeds at 1200 UTC 1 May 2020 from Great Plains stations in the NWS rawinsonde network. A station is listed if the low-level speed maximum and rate of decrease of speed above the maximum satisfied the Bonner (1968) criteria for the definition/classification of a low-level jet. The peak speed is in m s⁻¹, the height of the peak speed ($z_{\rm max}$) is in m AGL, and the direction of the wind maximum (DIR) is in degrees. If the peak speed occurred at multiple adjacent levels, the lower of the heights was chosen for $z_{\rm max}$.

Station ID	Location	Peak speed	DIR	z_{max}	Bonner category
KDRT	Del Rio, TX	18.0	170	472	2
KMAF	Midland, TX	18.0	200	347	2
KFWD	Fort Worth, TX	19.5	205	597	2
KAMA	Amarillo, TX	17.0	260	365	2
KOUN	Norman, OK	23.7	225	557	3
KDDC	Dodge City, KS	12.3	250	429	1
KTOP	Topeka, KS	19.5	200	340	2
KOAX	Omaha, NE	18.5	180	260	2
KABR	Aberdeen, SD	19.5	200	518	2

 v_g was problematic; unlike u, the v component did not level off with height in the free atmosphere. Based on ERA5 winds in the 500–600-hPa layer 6 , we took $u_g=10~{\rm m~s}^{-1}$ and $v_g=-10~{\rm m~s}^{-1}$. The parameter values used in this test are given in Table 5.

Time-height plots of the analytical model winds (Fig. 12) showed that the nighttime peak values of u, v, and speed, and the times and heights of these maxima were very similar to those seen in the lidar data (Fig. 10). The analytical model winds were also in good agreement with the ERA5 winds at 1000 UTC 1 May 2020 (Fig. 11, and discussion above), when the jet was near its peak intensity. In the analytical model, v peaked at 26.6 m s⁻¹ at height 320 m, the westerly wind (u > 0) peaked at 20.5 m s⁻¹ at height 560 m, and the lowlevel easterly wind (u < 0) peaked at -6.0 m s^{-1} at height 140 m, while in the lidar data, v peaked at 25 m s⁻¹ at height 560 m, the westerly wind peaked at 20 m s⁻¹ at height 760 m, and the low-level easterly wind peaked at -7 m s^{-1} at height 140 m. Although the peak speed in the model (28 m s⁻¹) was close to that in the lidar data (29 m s⁻¹), the model did not capture the double peak in the lidar data. Instead, the model produced a single lobe of winds near peak intensity roughly from the time the v-wind peaked to the time the u-wind peaked. Additionally, although the heights of the peak nighttime v and wind speed in the lidar data are similar to those predicted by the analytical model, the behavior of the heights in the hours leading up to their nighttime peaks are different, with ascent observed in the lidar data, but descent followed by a levelling off seen in the analytical model.

⁶ In their analyses of southern Great Plains NLLJs, Parish (2016, 2017) and Parish and Clark (2017) considered the 600-hPa surface to be in the free atmosphere.

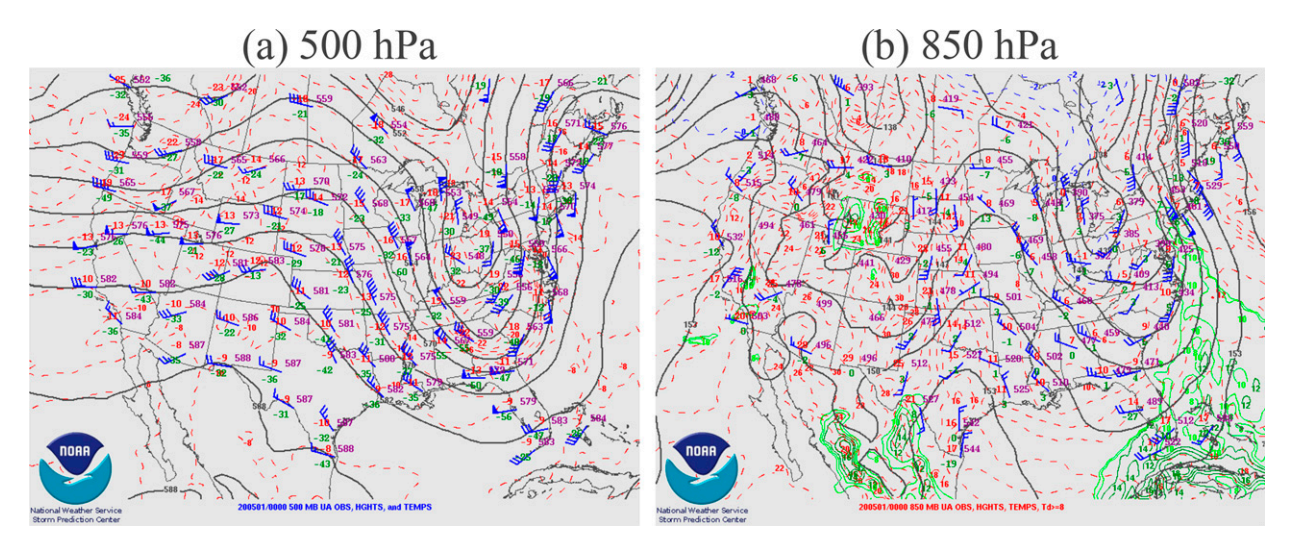


Fig. 7. NOAA/NWS/SPC geopotential height, temperature, and wind analyses for 0000 UTC 1 May 2020 at (a) 500 and (b) 850 hPa.

6. Conclusions

An analytical model was developed for the emergence of a Blackadar-like IO/NLLJ (with provision for reduced but nonzero nighttime turbulence) from a broad baroclinic zone over flat terrain. The surface buoyancy was specified to vary linearly with a horizontal coordinate (constant surface buoyancy gradient), and the eddy viscosity and eddy diffusivity were specified to increase abruptly at sunrise and decrease abruptly at sunset. The net horizontal PGF arising

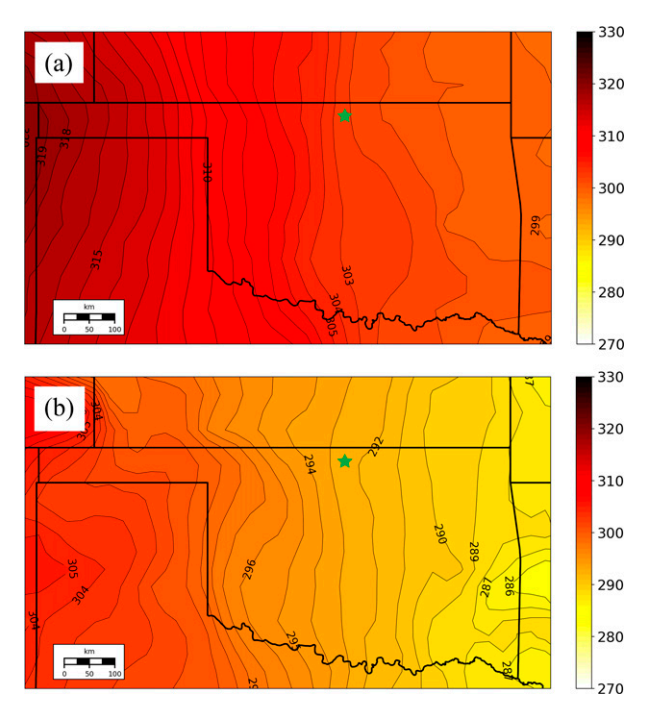


FIG. 8. ERA5 surface analyses of θ_{ν} (K) at (a) 2200 UTC 30 Apr and (b) 1000 UTC 1 May 2020. Contour interval is 1 K. Green star marks the ARM SGP central facility near Lamont, OK.

from contributions by the free-atmosphere PGF and the PGF associated with the buoyancy gradient provided a good background state on which the Blackadar IO/NLLJ mechanism could operate. A particularly large net PGF could be obtained when the free-atmosphere PGF and the low-level buoyancy gradient pointed in the same direction (e.g., westward during the warm season over the Great Plains).

The spatial ansatzes for the wind, pressure, and buoyancy fields used in the analytical model reduced the equations of motion, thermal energy, and mass conservation to a system of 1D (in height) partial differential equations. Diurnally periodic solutions of these reduced equations were obtained analytically. The solutions depended on the surface buoyancy gradient, Coriolis parameter, free-atmosphere geostrophic wind, a radiative damping parameter, time of sunset, and the temporal characteristics of the eddy viscosity and eddy diffusivity coefficients.

In a series of southerly NLLJ sensitivity experiments, the model solutions displayed the hallmarks of Blackadar-like IO/NLLJs: a sudden acceleration of the low-level winds following a sharp reduction in the turbulent mixing at sunset, anticyclonic rotation of the winds through the night, and peak wind speeds obtained within a few hours of (after) local midnight. The model also predicted that, unlike the daytime surface buoyancy gradient, which exerted a large impact on the strength of the NLLJ winds, the nighttime surface buoyancy gradient had little effect on jet strength. In farther southerly jet experiments that focused on purely baroclinic forcing (free-atmosphere geostrophic wind was set to zero), the peak NLLJ winds were more sensitive to the nighttime eddy viscosity ν_n than the nighttime eddy diffusivity κ_n . Consistent with B57 and S16, the stronger jets in these NOGEOS experiments were associated with smaller ν_n (larger day-to-night ratio of eddy viscosity). Additional NOGEOS-type experiments predicted that jet strength was more sensitive to the daytime eddy diffusivity κ_d than the daytime eddy viscosity ν_d , with

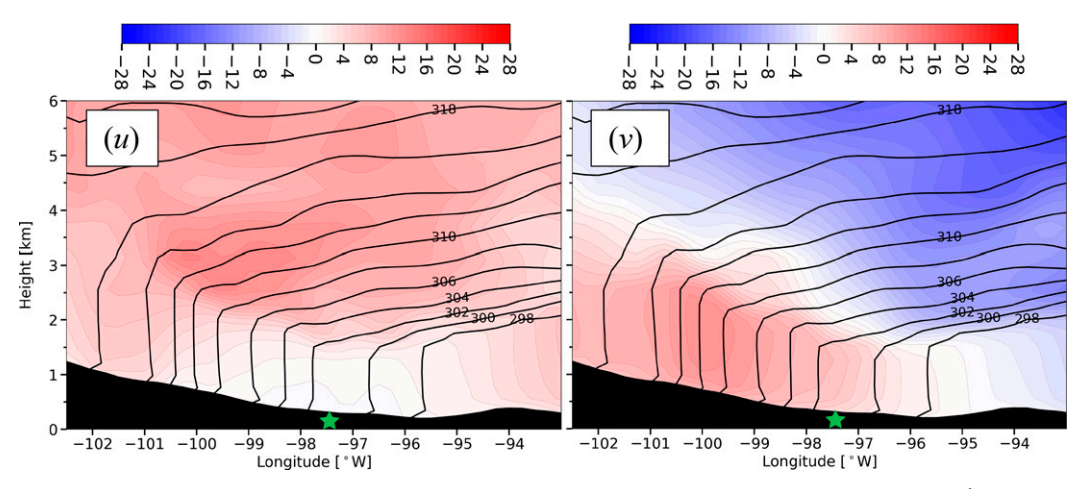


FIG. 9. Vertical cross section of ERA5 fields through 36.5°N at 2200 UTC 30 Apr 2020: (left) u (m s⁻¹), (right) v (m s⁻¹), and (both panels) θ_v (K). Color shading displays u and v at 1 m s⁻¹ intervals. Bold solid lines depict θ_v at 2-K intervals. Green star marks the ARM SGP central facility.

stronger jets associated with larger κ_d . However intriguing, some of these sensitivities might be outcomes of our highly simplified treatment of turbulence and other physical processes. It may be best to explore these sensitivities further

numerically, using the tools of large-eddy simulation or DNS.

The utility of the analytical model for describing real world NLLJs generated by a broad baroclinic zone was

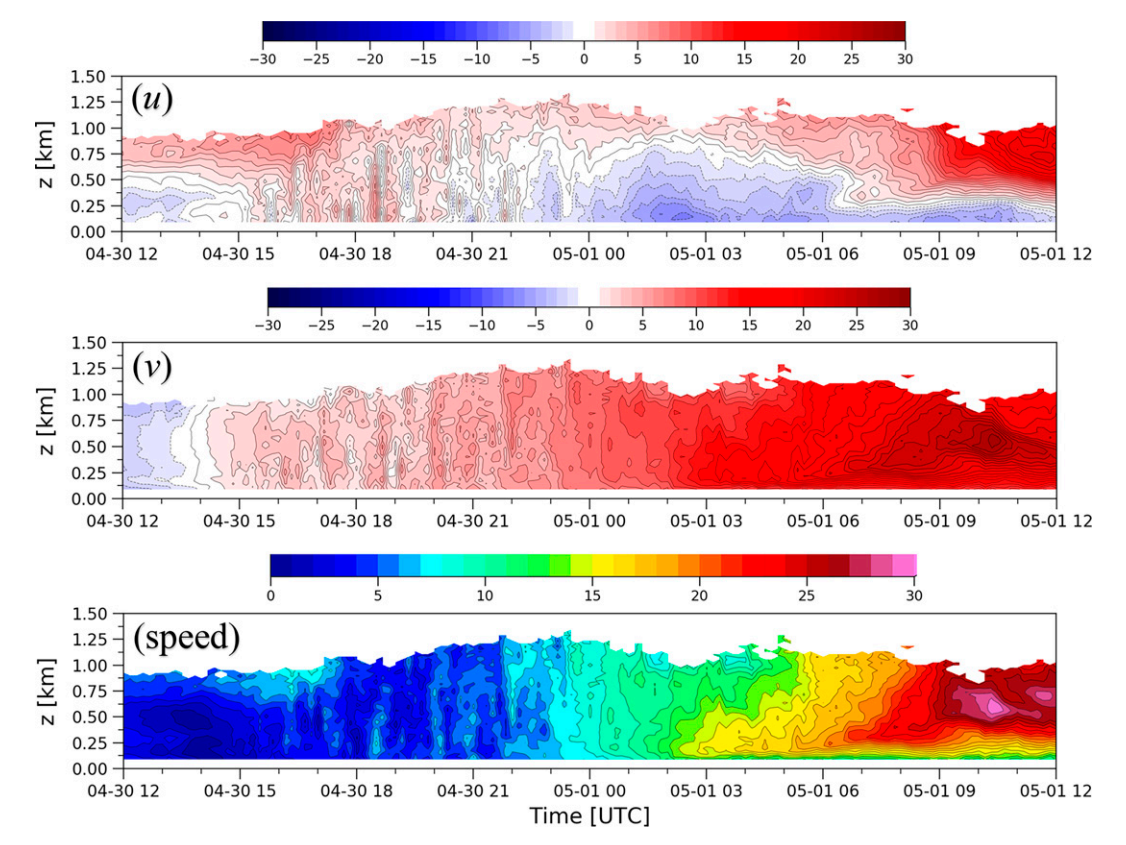


FIG. 10. Time-height plots of (top) u (m s⁻¹), (middle) v (m s⁻¹), and (bottom) wind speed (m s⁻¹) from a Doppler lidar at the ARM SGP central facility for the 24-h period starting near sunrise on 30 Apr 2020. Sunrise is at 1139 UTC. Sunset is at 0118 UTC.

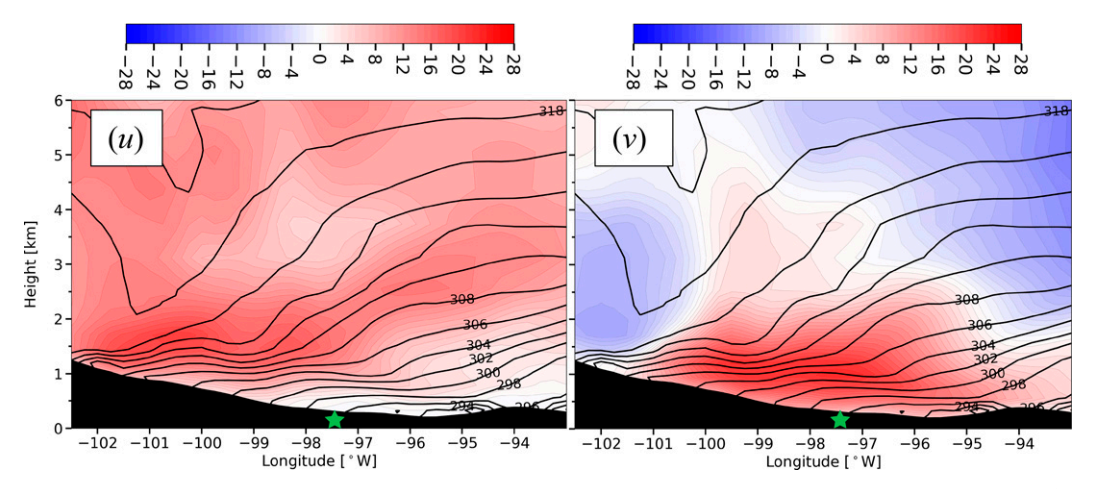


FIG. 11. Vertical cross section of ERA5 fields through 36.5°N at 1000 UTC 1 May 2020: (left) u (m s⁻¹), (right) v (m s⁻¹), and (both panels) θ_v (K). Color shading displays u and v at 1 m s⁻¹ intervals. Bold solid lines depict θ_v at 2-K intervals. Green star marks the ARM SGP central facility.

demonstrated for an NLLJ that developed over the Great Plains on 1 May 2020. The peak nighttime values of u, v, and speed, and the times and heights of these maxima from the model were in remarkably close agreement with those seen in lidar data from the ARM SGP central facility near Lamont, Oklahoma. However, the agreement may have been somewhat fortuitous given the model parameter sensitivities noted for the southerly jet experiments and the overall model simplicity, viz., mixing coefficients that are independent of height, morning and evening transitions that are nearly instantaneous, a surface buoyancy that varies linearly spatially, and a free atmosphere that is barotropic and in a geostrophic balance. We also note that, although the lidar-observed heights of the nighttime v-wind and wind speed maxima are similar to those predicted by the analytical model, the behaviors of these heights in the hours leading up to the nighttime peaks are different, with increases seen in the lidar data, but decreases and then a levelling off seen in the analytical model.

Questions about baroclinic NLLJs over the Great Plains remain. What factors underpin westward increases in the surface buoyancy? To what extent do these factors affect each other? How might these factors and the feedbacks between them change under various synoptic settings and climate

TABLE 5. Parameter settings for the 1 May 2020 test case. Time of sunset (t_{set}) is in hours after sunrise.

Parameter	Value		
\overline{f}	$8.7 \times 10^{-5} \text{ s}^{-1} \text{ (lat } \approx 36.5^{\circ}\text{N)}$		
b_{xs}	$-6 \times 10^{-7} \text{ s}^{-2}$		
$t_{ m set}$	13.6 h		
ν_d, κ_d	$50 \text{ m}^2 \text{ s}^{-1}$		
ν_n , κ_n	$1 \text{ m}^2 \text{ s}^{-1}$		
u_g	10 m s^{-1}		
$oldsymbol{v}_g$ $oldsymbol{\delta}$	-10 m s^{-1}		
δ	$0.2 \mathrm{day}^{-1}$		

change scenarios? Based on the climatological westward decrease of rainfall over the region, one might expect an eastward-directed soil moisture gradient to play a role in establishing the surface buoyancy gradient. However, as noted by Gebauer and Shapiro (2019), while the Great Plains NLLJs are most frequent during the warm season, the soil moisture gradient in this region is actually weakest during that period. Other processes to explore include radiative effects, boundary layer turbulence, differential advection of heat

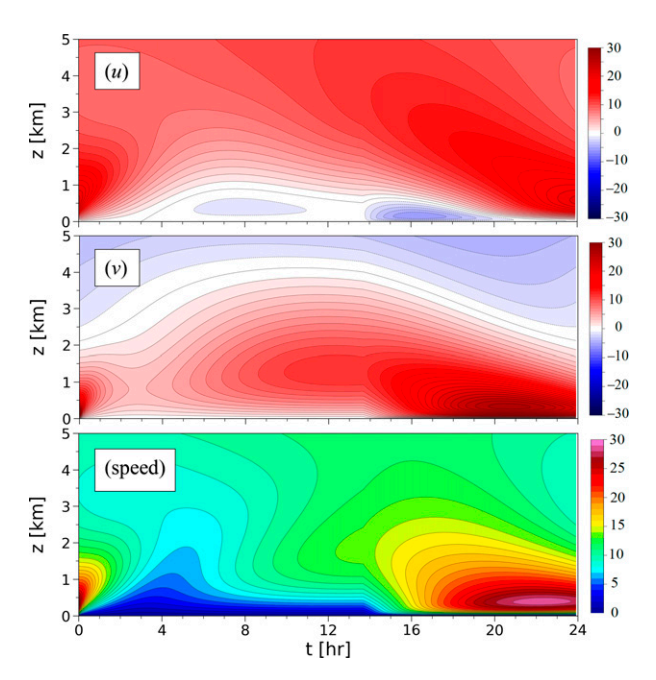


FIG. 12. Time–height plots of the analytical model winds for the 1 May 2020 test case: (top) u (m s⁻¹), (middle) v (m s⁻¹), and (bottom) wind speed (m s⁻¹). Time (t) is in hours after sunrise. Sunrise (t = 0 h) is at 1139 UTC 30 Apr 2020. Sunset (t \approx 13.6 h) is at 0118 UTC 1 May 2020. Parameter settings are given in Table 4.

and momentum, differential surface roughness, and differential surface-atmosphere fluxes of heat and moisture.

Acknowledgments. This research was supported by NSF AGS-1921587. The authors thank the anonymous reviewers for their constructive comments and Chris Rattray for discussions about the Great Plains environment and the behavior of NLLJs during IHOP_2002. Comments by Don Huston on an earlier draft led to an improved presentation. Shawn Riley and David Goines provided computing assistance.

Data availability statement. The analytical model code is available from the lead author upon request.

REFERENCES

- Allen, C. J. T., and R. Washington, 2014: The low-level jet dust emission mechanism in the central Sahara: Observations from Bordj-Badji Mokhtar during the June 2011 Fennec Intensive Observation Period. J. Geophys. Res. Atmos., 119, 2990–3015, https://doi.org/10.1002/2013JD020594.
- Andreas, E. L, K. J. Claffey, and A. P. Makshtas, 2000: Low-level atmospheric jets and inversions over the Western Weddell Sea. *Bound.-Layer Meteor.*, 97, 459–486, https://doi.org/10. 1023/A:1002793831076.
- Anthes, R. A., Y.-H. Kuo, S. G. Benjamin, and Y.-F. Li, 1982: The evolution of the mesoscale environment of severe local storms: Preliminary modeling results. *Mon. Wea. Rev.*, **110**, 1187–1213, https://doi.org/10.1175/1520-0493(1982)110<1187: TEOTME>2.0.CO:2.
- Aristov, S. N., and P. G. Frik, 1988: Large-scale turbulence in a thin layer of nonisothermal rotating fluid. *Fluid Dyn.*, 23, 522–528, https://doi.org/10.1007/BF01055074.
- ARM, 2010: Doppler Lidar Profiles (DLPROFWIND4NEWS): 2010-11-02 to 2021-02-09. Southern Great Plains (SGP) Central Facility, Lamont, OK (C1), ARM Data Center, Data (Basel), (set), accessed 16 February 2021, http://dx.doi.org/10.5439/1190027.
- Arritt, R. W., T. D. Rink, M. Segal, D. P. Todey, C. A. Clark, M. J. Mitchell, and K. M. Labas, 1997: The Great Plains low-level jet during the warm season of 1993. *Mon. Wea. Rev.*, 125, 2176–2192, https://doi.org/10.1175/1520-0493(1997)125 <2176:TGPLLJ>2.0.CO;2.
- Baas, P., F. C. Bosveld, H. Klein Baltink, and A. A. M. Holtslag, 2009: A climatology of low-level jets at Cabauw. J. Appl. Meteor. Climatol., 48, 1627–1642, https://doi.org/10.1175/2009JAMC1965.1.
- Banta, R. M., 2008: Stable-boundary-layer regimes from the perspective of the low-level jet. *Acta Geophys.*, 56, 58–87, https://doi.org/10.2478/s11600-007-0049-8.
- —, and Coauthors, 1998: Daytime buildup and nighttime transport of urban ozone in the boundary layer during a stagnation episode. *J. Geophys. Res.*, 103, 22519–22544, https://doi.org/10.1029/98JD01020.
- —, R. K. Newsom, J. K. Lundquist, Y. L. Pichugina, R. L. Coulter, and L. Mahrt, 2002: Nocturnal low-level jet characteristics over Kansas during CASES-99. *Bound.-Layer Meteor.*, 105, 221–252, https://doi.org/10.1023/A:1019992330866.
- —, Y. L. Pichugina, N. D. Kelley, B. Jonkman, and W. A. Brewer, 2008: Doppler lidar measurements of the Great Plains low-level jet: Applications to wind energy. *IOP Conf.*

- Ser. Earth Environ. Sci., 1, 012020, https://doi.org/10.1088/1755-1315/1/1/012020.
- —, —, R. M. Hardesty, and W. A. Brewer, 2013: Wind energy meteorology: Insight into wind properties in the turbine-rotor layer of the atmosphere from high-resolution Doppler lidar. *Bull. Amer. Meteor. Soc.*, **94**, 883–902, https://doi.org/10.1175/BAMS-D-11-00057.1.
- Bao, J. W., S. A. Michelson, P. O. G. Persson, I. V. Djalalova, and J. M. Wilczak, 2008: Observed and WRF-simulated low-level winds in a high-ozone episode during the Central California Ozone Study. *J. Appl. Meteor. Climatol.*, 47, 2372–2394, https://doi.org/10.1175/2008JAMC1822.1.
- Benjamin, S. G., and T. N. Carlson, 1986: Some effects of surface heating and topography on the regional severe storm environment. Part I: Three-dimensional simulations. *Mon. Wea. Rev.*, **114**, 307–329, https://doi.org/10.1175/1520-0493(1986)114 <0307:SEOSHA>2.0.CO:2.
- Berg, L. K., L. D. Riihimaki, Y. Qian, H. Yan, and M. Huang, 2015: The low-level jet over the southern Great Plains determined from observations and reanalyses and its impact on moisture transport. J. Climate, 28, 6682–6706, https://doi.org/ 10.1175/JCLI-D-14-00719.1.
- Beyrich, F., D. Kalass, and U. Weisensee, 1997: Influence of the nocturnal low-level jet on the vertical and mesoscale structure of the stable boundary layer as revealed from Dopplersodar-observations. Acoustic Remote Sensing Applications, S. P. Singal, Ed., Narosa Publishing House, 236–246.
- Blackadar, A. K., 1957: Boundary layer wind maxima and their significance for the growth of nocturnal inversions. *Bull. Amer. Meteor. Soc.*, 38, 283–290, https://doi.org/10.1175/1520-0477-38.5.283.
- Bonin, T. A., P. M. Klein, and P. B. Chilson, 2020: Contrasting characteristics and evolution of southerly low-level jets during different boundary-layer regimes. *Bound.-Layer Meteor.*, 174, 179–202, https://doi.org/10.1007/s10546-019-00481-0.
- Bonner, W. D., 1968: Climatology of the low level jet. *Mon. Wea. Rev.*, **96**, 833–850, https://doi.org/10.1175/1520-0493(1968)096 <0833:COTLLJ>2.0.CO;2.
- —, and J. Paegle, 1970: Diurnal variations in boundary layer winds over the south- central United States in summer. *Mon. Wea. Rev.*, 98, 735–744, https://doi.org/10.1175/1520-0493 (1970)098<0735:DVIBLW>2.3.CO;2.
- Brook, R. R., 1985: The Koorin nocturnal low-level jet. *Bound-Layer Meteor.*, **32**, 133–154, https://doi.org/10.1007/BF00120932.
- Buajitti, K., and A. K. Blackadar, 1957: Theoretical studies of diurnal wind-structure variations in the planetary boundary layer. *Quart. J. Roy. Meteor. Soc.*, 83, 486–500, https://doi.org/ 10.1002/qj.49708335804.
- Businger, J. A., J. C. Wyngaard, Y. Izumi, and E. F. Bradley, 1971: Flux-profile relationships in the atmospheric surface layer. J. Atmos. Sci., 28, 181–189, https://doi.org/10.1175/1520-0469(1971)028<0181:FPRITA>2.0.CO;2.
- Carlson, T. N., and F. H. Ludlam, 1968: Conditions for the occurrence of severe local storms. *Tellus*, 20, 203–226, https://doi.org/10.3402/tellusa.v20i2.10002.
- Carroll, B. J., B. B. Demoz, and R. Delgado, 2019: An overview of low-level jet winds and corresponding mixed layer depths during PECAN. J. Geophys. Res. Atmos., 124, 9141–9160, https://doi.org/10.1029/2019JD030658.
- Chandler, C., P. Cheney, P. Thomas, L. Trabaud, and D. Williams, 1991: Fire in forestry. *Forest Fire Behavior and Effects*, Vol. 1, Krieger Publishing Co., 441 pp.

- Charney, J. J., X. Bian, B. E. Potter, and W. E. Heilman, 2003: Low level jet impacts on fire evolution in the Mack Lake and other severe wildfires. Fifth Symp. on Fire and Forest Meteorology/Second Int. Wildland Fire Ecology and Fire Management Congress, Orlando, FL, Amer. Meteor. Soc., 1.5.
- Chen, G., W. Sha, T. Iwasaki, and Z. Wen, 2017: Diurnal cycle of a heavy rainfall corridor over East Asia. *Mon. Wea. Rev.*, **145**, 3365–3389, https://doi.org/10.1175/MWR-D-16-0423.1.
- Corsmeier, U., N. Kalthoff, O. Kolle, M. Kotzian, and F. Fiedler, 1997: Ozone concentration jump in the stable nocturnal boundary-layer during a LLJ-event. *Atmos. Environ.*, 31, 1977–1989, https://doi.org/10.1016/S1352-2310(96)00358-5.
- Cosack, N., S. Emeis, and M. Kühn, 2007: On the influence of low-level jets on energy production and loading of wind turbines. Wind Energy, J. Peinke, P. Schaumann, and S. Barth, Eds., Springer, https://doi.org/10.1007/978-3-540-33866-6_61.
- Dandou, A., M. Tombrou, K. Schäfer, S. Emeis, A. P. Protonotariou, E. Bossioli, N. Soulakellis, and P. Suppan, 2009: A comparison between modelled and measured mixing-layer height over Munich. *Bound.-Layer Meteor.*, 131, 425–440, https:// doi.org/10.1007/s10546-009-9373-7.
- Dentoni, M. C., G. E. Defossé, J. C. Labraga, and H. F. del Valle, 2001: Atmospheric and fuel conditions related to the Puerto Madryn fire of 21 January, 1994. *Meteor. Appl.*, 8, 361–370, https://doi.org/10.1017/S1350482701003127.
- Drake, V. A., and R. A. Farrow, 1988: The influence of atmospheric structure and motions on insect migration. *Annu. Rev. Entomol.*, 33, 183–210, https://doi.org/10.1146/annurev.en.33.010188.001151.
- Du, Y., and G. Chen, 2019: Climatology of low-level jets and their impact on rainfall over southern China during the early-summer rainy season. J. Climate, 32, 8813–8833, https://doi.org/10. 1175/JCLI-D-19-0306.1.
- —, Q. Zhang, Y. Ying, and Y. Yang, 2012: Characteristics of low-level jets in Shanghai during the 2008–2009 warm seasons as inferred from wind profiler radar data. *J. Meteor. Soc. Japan*, 90, 891–903, https://doi.org/10.2151/jmsj.2012-603.
- —, Y.-L. Chen, Y. Zhao, and X. Wang, 2014: Numerical simulations of spatial distributions and diurnal variations of low-level jets in China during early summer. *J. Climate*, 27, 5747–5767, https://doi.org/10.1175/JCLI-D-13-00571.1.
- Egger, J., 1985: Slope winds and the axisymmetric circulation over Antarctica. *J. Atmos. Sci.*, **42**, 1859–1867, https://doi.org/10. 1175/1520-0469(1985)042<1859:SWATAC>2.0.CO;2.
- Emeis, S., 2013: Wind Energy Meteorology: Atmospheric Physics for Wind Power Generation. Springer, 196 pp.
- Fiedler, B. H., 1999: Thermal convection in a layer bounded by uniform heat flux: Application of a strongly nonlinear analytical solution. *Geophys. Astrophys. Fluid Dyn.*, 91, 223–250, https://doi.org/10.1080/03091929908203705.
- Fiedler, S., K. Schepanski, B. Heinold, P. Knippertz, and I. Tegen, 2013: Climatology of nocturnal low-level jets over North Africa and implications for modeling mineral dust emission. *J. Geophys. Res. Atmos.*, 118, 6100–6121, https://doi.org/10. 1002/jgrd.50394.
- French, A. J., and M. D. Parker, 2010: The response of simulated nocturnal convective systems to a developing low-level jet. *J. Atmos. Sci.*, **67**, 3384–3408, https://doi.org/10.1175/2010JAS3329.1.
- Ge, J. M., H. Liu, J. Huang, and Q. Fu, 2016: Taklimakan Desert nocturnal low-level jet: Climatology and dust activity. Atmos. Chem. Phys., 16, 7773–7783, https://doi.org/10.5194/acp-16-7773-2016.

- Gebauer, J. G., and A. Shapiro, 2019: Clarifying the baroclinic contribution to the Great Plains low-level jet frequency maximum. *Mon. Wea. Rev.*, **147**, 3481–3493, https://doi.org/10. 1175/MWR-D-19-0024.1.
- —, E. Fedorovich, and P. Klein, 2018: Convection initiation caused by heterogeneous low-level jets over the Great Plains. *Mon. Wea. Rev.*, **146**, 2615–2637, https://doi.org/10.1175/MWR-D-18-0002.1.
- Gibson, M. M., and B. E. Launder, 1978: Ground effects on pressure fluctuations in the atmospheric boundary layer. *J. Fluid Mech.*, 86, 491–511, https://doi.org/10.1017/S0022112078001251.
- Gutman, L. N., 1972: Introduction to the Nonlinear Theory of Mesoscale Meteorological Processes. Israel Program for Scientific Translations, 224 pp.
- Hart, J. E., 1972: Stability of thin non-rotating Hadley circulations.
 J. Atmos. Sci., 29, 687–697, https://doi.org/10.1175/1520-0469
 (1972)029<0687:SOTNRH>2.0.CO;2.
- Heinold, B., P. Knippertz, J. Marsham, S. Fiedler, N. Dixon, K. Schepanski, B. Laurent, and I. Tegen, 2013: The role of deep convection and nocturnal low-level jets for dust emission in summertime West Africa: Estimates from convectionpermitting simulations. J. Geophys. Res. Atmos., 118, 4385– 4400, https://doi.org/10.1002/jgrd.50402.
- Hersbach, H., and Coauthors, 2020: The ERA5 global reanalysis. *Quart. J. Roy. Meteor. Soc.*, **146**, 1999–2049, https://doi.org/10.1002/qj.3803.
- Higgins, R. W., Y. Yao, E. S. Yaresh, J. E. Janowiak, and K. C. Mo, 1997: Influence of the Great Plains low-level jet on summertime precipitation and moisture transport over the central United States. *J. Climate*, 10, 481–507, https://doi.org/10. 1175/1520-0442(1997)010<0481:IOTGPL>2.0.CO;2.
- Hoecker, W. H., 1963: Three southerly low-level jet systems delineated by the Weather Bureau special pibal network of 1961. *Mon. Wea. Rev.*, **91**, 573–582, https://doi.org/10.1175/1520-0493(1963)091<0573:TSLJSD>2.3.CO;2.
- ——, 1965: Comparative physical behavior of southerly boundary-layer wind jets. *Mon. Wea. Rev.*, **93**, 133–144, https://doi.org/10.1175/1520-0493(1965)093<0133:CPBOSB>2.3.CO;2.
- Holton, J. R., 1967: The diurnal boundary layer wind oscillation above sloping terrain. *Tellus*, 19A, 199–205, https://doi.org/10. 1111/j.2153-3490.1967.tb01473.x.
- Howell, J. F., and J. Sun, 1999: Surface-layer fluxes in stable conditions. *Bound.-Layer Meteor.*, **90**, 495–520, https://doi.org/10.1023/A:1001788515355.
- Ingel, L. Kh., 1996: Approximate analytical solution of the nonlinear problem of a flow over a thermally inhomogeneous underlying surface. *Meteor. Atmos. Phys.*, 58, 13–19, https://doi.org/10.1007/BF01027553.
- Isard, S. A., and S. H. Gage, 2001: Flow of Life in the Atmosphere: An Airscape Approach to Understanding Invasive Organisms. Michigan State University Press, 240 pp.
- Kallistratova, M. A., and R. D. Kouznetsov, 2012: Low-level jets in the Moscow region in summer and winter observed with a sodar network. *Bound.-Layer Meteor.*, 143, 159–175, https:// doi.org/10.1007/s10546-011-9639-8.
- Kitamura, Y., A. Hori, and T. Yagi, 2013: Flux Richardson number and turbulent Prandtl number in a developing stable boundary layer. J. Meteor. Soc. Japan, 91, 655–666, https://doi.org/10.2151/jmsj.2013-507.
- Klein, P. M., X.-M. Hu, and M. Xue, 2014: Impacts of mixing processes in nocturnal atmospheric boundary layer on urban ozone concentrations. *Bound.-Layer Meteor.*, 150, 107–130, https://doi.org/10.1007/s10546-013-9864-4.

- —, —, A. Shapiro, and M. Xue, 2016: Linkages between boundary-layer structure and development of nocturnal low-level jets in central Oklahoma. *Bound.-Layer Meteor.*, **158**, 383–408, https://doi.org/10.1007/s10546-015-0097-6.
- Knippertz, P., and M. C. Todd, 2012: Mineral dust aerosols over the Sahara: Meteorological controls on emission and transport and implications for modeling. *Rev. Geophys.*, 50, RG1007, https://doi.org/10.1029/2011RG000362.
- Kurbatskiy, A. F., and L. I. Kurbatskaya, 2011: Efficiency of eddy mixing in a stable stratified atmospheric boundary layer. J. Appl. Mech. Tech. Phys., 52, 883–888, https://doi.org/10.1134/ S0021894411060058.
- La Sorte, F. A., and Coauthors, 2014: The role of atmospheric conditions in the seasonal dynamics of North American migration flyways. *J. Biogeogr.*, 41, 1685–1696, https://doi.org/ 10.1111/jbi.12328.
- Lackmann, G. M., 2002: Cold-frontal potential vorticity maxima, the low-level jet, and moisture transport in extratropical cyclones. *Mon. Wea. Rev.*, 130, 59–74, https://doi.org/10.1175/ 1520-0493(2002)130<0059:CFPVMT>2.0.CO;2.
- Lilly, D. K., 1978: A severe downslope windstorm and aircraft turbulence induced by a mountain wave. *J. Atmos. Sci.*, **35**, 59–77, https://doi.org/10.1175/1520-0469(1978)035<0059: ASDWAA>2.0.CO;2.
- Lindley, T. T., D. A. Speheger, M. A. Day, G. P. Murdoch, B. R. Smith, N. J. Nauslar, and D. C. Daily, 2019: Megafires on the southern Great Plains. J. Oper. Meteor., 7, 164–179, https://doi.org/10.15191/nwajom.2019.0712.
- Macklin, S. A., N. A. Bond, and J. P. Walker, 1990: Structure of a low-level jet over lower Cook Inlet, Alaska. *Mon. Wea. Rev.*, 118, 2568–2578, https://doi.org/10.1175/1520-0493(1990)118 <2568:SOALLJ>2.0.CO:2.
- Mahrt, L., and D. Vickers, 2005: Extremely weak mixing in stable conditions. *Bound.-Layer Meteor.*, 119, 19–39, https://doi.org/ 10.1007/s10546-005-9017-5.
- Mao, H., and R. Talbot, 2004: Role of meteorological processes in two New England ozone episodes during summer 2001.
 J. Geophys. Res., 109, D20305, https://doi.org/10.1029/ 2004JD004850.
- Medelfef, A., D. Henry, A. Bouabdallah, S. Kaddeche, and R. Boussaa, 2017: Effect of rotation on the stability of sideheated buoyant convection between infinite horizontal walls. *Phys. Rev. Fluids*, 2, 093902, https://doi.org/10.1103/ PhysRevFluids.2.093902.
- Mercier, J. F., and C. Normand, 1996: Buoyant-thermocapillary instabilities of differentially heated liquid layers. *Phys. Fluids*, 8, 1433–1445, https://doi.org/10.1063/1.868920.
- Miao, Y., S. Liu, L. Sheng, S. Huang, and J. Li, 2019: Influence of boundary layer structure and low-level jet on PM2.5 pollution in Beijing: A case study. *Int. J. Environ. Res. Pub. Health*, 16, 616, https://doi.org/10.3390/ijerph16040616.
- Monaghan, A. J., D. L. Rife, J. O. Pinto, C. A. Davis, and J. R. Hannan, 2010: Global precipitation extremes associated with diurnally varying low-level jets. *J. Climate*, 23, 5065–5084, https://doi.org/10.1175/2010JCLI3515.1.
- Oliveira, M. I., E. L. Nascimento, and C. Kannenberg, 2018: A new look at the identification of low-level jets in South America. *Mon. Wea. Rev.*, **146**, 2315–2334, https://doi.org/10.1175/MWR-D-17-0237.1.
- Parish, T. R., 2016: A comparative study of the 3 June 2015 Great Plains low-level jet. *Mon. Wea. Rev.*, **144**, 2963–2979, https://doi.org/10.1175/MWR-D-16-0071.1.

- ——, 2017: On the forcing of the summertime Great Plains low-level jet. J. Atmos. Sci., 74, 3937–3953, https://doi.org/10.1175/JAS-D-17-0059.1.
- —, and L. D. Oolman, 2010: On the role of sloping terrain in the forcing of the Great Plains low-level jet. *J. Atmos. Sci.*, **67**, 2690–2699, https://doi.org/10.1175/2010JAS3368.1.
- —, and R. D. Clark, 2017: On the initiation of the 20 June 2015 Great Plains low-level jet. *J. Appl. Meteor. Climatol.*, **56**, 1883–1895, https://doi.org/10.1175/JAMC-D-16-0187.1.
- —, A. R. Rodi, and R. D. Clark, 1988: A case study of the summertime Great Plains low level jet. *Mon. Wea. Rev.*, **116**, 94–105, https://doi.org/10.1175/1520-0493(1988)116<0094: ACSOTS>2.0.CO;2.
- —, R. D. Clark, and T. D. Sikora, 2020: Nocturnal destabilization associated with the summertime Great Plains low-level jet. *Mon. Wea. Rev.*, 148, 4641–4656, https://doi.org/10.1175/MWR-D-19-0394.1.
- Parsons, D. B., M. A. Shapiro, R. M. Hardesty, R. J. Zamora, and J. M. Intrieri, 1991: The finescale structure of a west Texas dryline. *Mon. Wea. Rev.*, **119**, 1242–1258, https://doi.org/10. 1175/1520-0493(1991)119<1242:TFSOAW>2.0.CO;2.
- —, and E. Miller, 2000: The mesoscale structure of a nocturnal dryline and of a frontal-dryline merger. *Mon. Wea. Rev.*, **128**, 3824–3838, https://doi.org/10.1175/1520-0493(2001) 129<3824:TMSOAN>2.0.CO;2.
- —, K. R. Haghi, K. T. Halbert, B. Elmer, and J. Wang, 2019: The potential role of atmospheric bores and gravity waves in the initiation and maintenance of nocturnal convection over the Southern Great Plains. *J. Atmos. Sci.*, **76**, 43–68, https:// doi.org/10.1175/JAS-D-17-0172.1.
- Pham, N. T., K. Nakamura, F. A. Furuzawa, and S. Satoh, 2008: Characteristics of low level jets over Okinawa in the Baiu and post-Baiu seasons revealed by wind profiler observations. *J. Meteor. Soc. Japan*, 86, 699–717, https://doi.org/10.2151/jmsj.86.699.
- Poulos, G., and S. Zhong, 2008: An observational history of small-scale katabatic winds in mid-latitudes. *Geogr. Compass*, **2**, 1798–1821, https://doi.org/10.1111/j.1749-8198.2008.00166.x.
- Reif, D. W., and H. B. Bluestein, 2017: A 20-year climatology of nocturnal convection initiation over the central and southern Great Plains during the warm season. *Mon. Wea. Rev.*, 145, 1615–1639, https://doi.org/10.1175/MWR-D-16-0340.1.
- —, and —, 2018: Initiation mechanisms of nocturnal convection without nearby surface boundaries over the central and southern Great Plains during the warm season. *Mon. Wea. Rev.*, **146**, 3053–3078, https://doi.org/10.1175/MWR-D-18-0040.1.
- Rife, D. L., J. O. Pinto, A. J. Monaghan, C. A. Davis, and J. R. Hannan, 2010: Global distribution and characteristics of diurnally varying low-level jets. *J. Climate*, 23, 5041–5064, https://doi.org/10.1175/2010JCLI3514.1.
- Schepanski, K., I. Tegen, M. C. Todd, B. Heinold, G. Boenisch, B. Laurent, and A. Macke, 2009: Meteorological processes forcing Saharan dust emission inferred from MSG-SEVIRI observations of subdaily dust source activation and numerical models. J. Geophys. Res., 114, D10201, https://doi.org/10. 1029/2008JD010325.
- Shamoun-Baranes, F. L., and W. M. G. Vansteelant, 2017: Atmospheric conditions create freeways, detours and tailbacks for migrating birds. *J. Comp. Physiol.*, 203A, 509–529, https://doi.org/10.1007/s00359-017-1181-9.

- Shapiro, A., and E. Fedorovich, 2007: Katabatic flow along a differentially cooled sloping surface. *J. Fluid Mech.*, 571, 149–175, https://doi.org/10.1017/S0022112006003302.
- —, and —, 2010: Analytical description of a nocturnal low-level jet. *Quart. J. Roy. Meteor. Soc.*, **136**, 1255–1262, https://doi.org/10.1002/qj.628.
- ——, and S. Rahimi, 2016: A unified theory for the Great Plains nocturnal low-level jet. *J. Atmos. Sci.*, **73**, 3037–3057, https://doi.org/10.1175/JAS-D-15-0307.1.
- ——, and J. G. Gebauer, 2018: Mesoscale ascent in nocturnal low-level jets. *J. Atmos. Sci.*, **75**, 1403–1427, https://doi.org/10.1175/JAS-D-17-0279.1.
- Sharan, M., and S. G. Gopalakrishnan, 1997: Comparative evaluation of eddy exchange coefficients for strong and weak wind stable boundary layer modeling. *J. Appl. Meteor.*, **36**, 545–559, https://doi.org/10.1175/1520-0450(1997)036<0545:CEOEEC>2. 0.CO:2.
- Shvarts, K. G., and A. Boudlal, 2010: Effect of rotation on stability of advective flow in horizontal liquid layer with a free upper boundary. J. Phys. Conf. Ser., 216, 012005, https://doi.org/10.1088/1742-6596/216/1/012005.
- Sladkovic, R., and H.-J. Kanter, 1977: Low-level jet in the Bavarian pre-alpine region. *Arch. Meteor. Geophys. Bioklimatol. Ser.*, **25A**, 343–355, https://doi.org/10.1007/BF02317994.
- Smith, M. K., and S. H. Davis, 1983a: Instabilities of dynamic thermocapillary liquid layers. Part 1. Convective instabilities. *J. Fluid Mech.*, 132, 119–144, https://doi.org/10.1017/ S0022112083001512.
- —, and —, 1983b: Instabilities of dynamic thermocapillary liquid layers. Part 2. Surface-wave instabilities. *J. Fluid Mech.*, **132**, 145–162, https://doi.org/10.1017/S0022112083001524.
- Smith, E. N., E. Fedorovich, and A. Shapiro, 2017: Comparison of analytical descriptions of nocturnal low-level jets within the Ekman model framework. *Environ. Fluid Mech.*, 17, 485–495, https://doi.org/10.1007/s10652-016-9502-z.
- —, J. G. Gebauer, P. M. Klein, E. Fedorovich, and J. A. Gibbs, 2019: The Great Plains low-level jet during PECAN: Observed and simulated characteristics. *Mon. Wea. Rev.*, **147**, 1845–1869, https://doi.org/10.1175/MWR-D-18-0293.1.
- Solomon, P., E. Cowling, G. Hidy, and C. Furiness, 2000: Comparison of scientific findings from major ozone field studies in North America and Europe. *Atmos. Environ.*, 34, 1885–1920, https://doi.org/10.1016/S1352-2310(99)00453-7.
- Song, J., K. Liao, R. L. Coulter, and B. M. Lesht, 2005: Climatology of the low-level jet at the Southern Great Plains Atmospheric Boundary Layer Experiments site. *J. Appl. Meteor.*, 44, 1593–1606, https://doi.org/10.1175/JAM2294.1.
- Stensrud, D. J., 1996: Importance of low-level jets to climate: A review. J. Climate, 9, 1698–1711, https://doi.org/10.1175/1520-0442(1996)009<1698:IOLLJT>2.0.CO;2.
- Storm, B., J. Dudhia, S. Basu, A. Swift, and I. Giammanco, 2009: Evaluation of the Weather Research and Forecasting model on forecasting low-level jets: Implications for wind energy. Wind Energy, 12, 81–90, https://doi.org/10.1002/we.288.
- Stull, R. B., 1988: An Introduction to Boundary Layer Meteorology. Kluwer, 666 pp.
- Sullivan, J. T., S. D. Rabenhorst, J. Dreessen, T. J. McGee, R. Delgado, L. Twigg, and G. Sumnicht, 2017: Lidar observations revealing transport of O₃ in the presence of a nocturnal low-level jet: Regional implications for "next-day" pollution. *Atmos. Environ.*, 158, 160–171, https://doi.org/10.1016/j.atmosenv.2017.03.039.

- Sun, W.-Y., and Y. Ogura, 1979: Boundary layer forcing as a possible trigger to squall line formation. *J. Atmos. Sci.*, **36**, 235–254, https://doi.org/10.1175/1520-0469(1979)036<0235: BLFAAP>2.0.CO;2.
- —, and C.-C. Wu, 1992: Formation and diurnal variation of the dryline. J. Atmos. Sci., 49, 1606–1619, https://doi.org/10.1175/ 1520-0469(1992)049<1606:FADVOT>2.0.CO;2.
- Todd, M. C., R. Washington, S. Raghavan, G. Lizcano, and P. Knippertz, 2008: Regional model simulations of the Bodélé low-level jet of northern Chad during the Bodélé Dust Experiment (BoDEx 2005). J. Climate, 21, 995–1012, https://doi.org/10.1175/2007JCL11766.1.
- Tombrou, M., A. Dandou, C. Helmis, E. Akylas, G. Angelopoulos, H. Flocas, V. Assimakopoulos, and N. Soulakellis, 2007: Model evaluation of the atmospheric boundary layer and mixed layer evolution. *Bound.-Layer Meteor.*, 124, 61–79, https://doi.org/10. 1007/s10546-006-9146-5.
- Trier, S. B., and D. B. Parsons, 1993: Evolution of environmental conditions preceding the development of a nocturnal mesoscale convective complex. *Mon. Wea. Rev.*, 121, 1078–1098, https://doi.org/10.1175/1520-0493(1993)121<1078:EOECPT>2. 0.CO:2.
- —, C. A. Davis, D. A. Ahijevych, M. L. Weisman, and G. H. Bryan, 2006: Mechanisms supporting long-lived episodes of propagating nocturnal convection within a 7-day WRF Model simulation. *J. Atmos. Sci.*, 63, 2437–2461, https://doi.org/10.1175/JAS3768.1.
- —, —, and R. E. Carbone, 2014: Mechanisms governing the persistence and diurnal cycle of a heavy rainfall corridor. *J. Atmos. Sci.*, 71, 4102–4126, https://doi.org/10.1175/JAS-D-14-0134.1.
- —, J. W. Wilson, D. A. Ahijevych, and R. A. Sobash, 2017: Mesoscale vertical motions near nocturnal convection initiation in PECAN. *Mon. Wea. Rev.*, **145**, 2919–2941, https://doi. org/10.1175/MWR-D-17-0005.1.
- Tuttle, J. D., and C. A. Davis, 2006: Corridors of warm season precipitation in the central United States. *Mon. Wea. Rev.*, 134, 2297–2317, https://doi.org/10.1175/MWR3188.1.
- Uccellini, L. W., and D. R. Johnson, 1979: The coupling of upper and lower tropospheric jet streaks and implications for the development of severe convective storms. *Mon. Wea. Rev.*, **107**, 682–703, https://doi.org/10.1175/1520-0493(1979)107<0682: TCOUAL>2.0.CO;2.
- Ueda, H., S. Mitsumoto, and S. Komori, 1981: Buoyancy effects on the turbulent transport processes in the lower atmosphere. *Quart. J. Roy. Meteor. Soc.*, 107, 561–578, https://doi.org/10. 1002/qj.49710745307.
- Van de Wiel, B. J. H., A. F. Moene, G. J. Steeneveld, P. Baas, F. C. Bosveld, and A. A. M. Holtslag, 2010: A conceptual view on inertial oscillations and nocturnal low-level jets. J. Atmos. Sci., 67, 2679–2689, https://doi.org/10.1175/2010JAS3289.1.
- Van Ulden, A. P., and J. Wieringa, 1996: Atmospheric boundary layer research at Cabauw. *Bound.-Layer Meteor.*, 78, 39–69, https://doi.org/10.1007/BF00122486.
- Vandenbussche, S., S. Callewaert, K. Schepanski, and M. De Mazière, 2020: North African mineral dust sources: New insights from a combined analysis based on 3D dust aerosol distributions, surface winds and ancillary soil parameters. *Atmos. Chem. Phys.*, 20, 15127–15146, https://doi.org/10.5194/acp-20-15127-2020.
- Wainwright, C. E., P. M. Stepanian, and K. G. Horton, 2016: The role of the U.S. Great Plains low-level jet in nocturnal

- migrant behavior. *Int. J. Biometeor.*, **60**, 1531–1542, https://doi.org/10.1007/s00484-016-1144-9.
- —, D. R. Reynolds, and A. M. Reynolds, 2020: Linking small-scale flight manoeuvers and density profiles to the vertical movement of insects in the nocturnal stable boundary layer. Sci. Rep., 10, 1019, https://doi.org/10.1038/s41598-020-57779-0.
- Walters, C. K., and J. A. Winkler, 2001: Airflow configurations of warm season southerly low-level wind maxima in the Great Plains. Part I: Spatial and temporal characteristics and relationship to convection. Wea. Forecasting, 16, 513–530, https:// doi.org/10.1175/1520-0434(2001)016<0513:ACOWSS>2. 0.CO:2.
- —, —, S. Husseini, R. Keeling, J. Nikolic, and S. Zhong, 2014: Low-level jets in the North American Regional Reanalysis (NARR): A comparison with rawinsonde observations. J. Appl. Meteor. Climatol., 53, 2093–2113, https://doi.org/10. 1175/JAMC-D-13-0364.1.
- Washington, R., and M. C. Todd, 2005: Atmospheric controls on mineral dust emission from the Bodélé Depression, Chad: The role of the low level jet. *Geophys. Res. Lett.*, 32, L17701, https://doi.org/10.1029/2005GL023597.
- —, S. Engelstaedter, S. M'Bainayel, and F. Mitchell, 2006: Dust and the low level circulation over the Bodélé depression, Chad: Observations from BoDEx 2005. *J. Geophys. Res.*, **111**, D03201, https://doi.org/10.1029/2005JD006502.
- Weckwerth, T. M., J. Hanesiak, J. W. Wilson, S. B. Trier, S. K. Degelia, W. A. Gallus Jr., R. D. Roberts, and X. Wang, 2019: Nocturnal convection initiation during PECAN 2015. *Bull. Amer. Meteor. Soc.*, 100, 2223–2239, https://doi.org/10.1175/BAMS-D-18-0299.1.
- Westbrook, J. K., 2008: Noctuid migration in Texas within the nocturnal aeroecological boundary layer. *Integr. Comp. Biol.*, **48**, 99–106, https://doi.org/10.1093/icb/icn040.
- ——, and S. A. Isard, 1999: Atmospheric scales of biotic dispersal. *Agric. For. Meteor.*, **97**, 263–274, https://doi.org/10.1016/ S0168-1923(99)00071-4.
- Wexler, H., 1961: A boundary layer interpretation of the low-level jet. *Tellus*, **13**, 368–378, https://doi.org/10.3402/tellusa.v13i3. 9513.

- Whiteman, C. D., X. Bian, and S. Zhong, 1997: Low-level jet climatology from enhanced rawinsonde observations at a site in the southern Great Plains. *J. Appl. Meteor.*, **36**, 1363–1376, https://doi.org/10.1175/1520-0450(1997)036<1363:LLJCFE>2. 0.CO;2.
- Wilczak, J. M., and Coauthors, 2019: The Second Wind Forecast Improvement Project (WFIP2): Observational field campaign. Bull. Amer. Meteor. Soc., 100, 1701–1723, https://doi. org/10.1175/BAMS-D-18-0035.1.
- Wolf, W. W., J. K. Westbrook, J. Raulston, S. D. Pair, and S. E. Hobbs, 1990: Recent airborne radar observations of migrant pests in the United States. *Philos. Trans. Roy. Soc. London*, 328B, 619–630, https://doi.org/10.1098/rstb.1990.0132.
- Wu, Y., and S. Raman, 1998: The summertime Great Plains low-level jet and the effect of its origin on moisture transport. Bound.-Layer Meteor., 88, 445–466, https://doi.org/10.1023/A: 1001518302649.
- Xue, M., X. Luo, K. Zhu, Z. Sun, and J. Fei, 2018: The controlling role of boundary layer inertial oscillations in Meiyu frontal precipitation and its diurnal cycles over China. *J. Geophys. Res.* Atmos., 123, 5090–5115, https://doi.org/10.1029/2018JD028368.
- Yamada, T., and G. Mellor, 1975: A simulation of the Wangara atmospheric boundary layer data. J. Atmos. Sci., 32, 2309–2329, https://doi.org/10.1175/1520-0469(1975)032<2309:ASOTWA>2. 0.CO:2.
- Zeng, W., G. Chen, Y. Du, and Z. Wen, 2019: Diurnal variations of low-level winds and precipitation response to large-scale circulations during a heavy rainfall event. *Mon. Wea. Rev.*, 147, 3981–4004, https://doi.org/10.1175/MWR-D-19-0131.1.
- Zhong, S., J. D. Fast, and X. Bian, 1996: A case study of the Great Plains low-level jet using wind profiler network data and a high-resolution mesoscale model. *Mon. Wea. Rev.*, **124**, 785–806, https://doi.org/10.1175/1520-0493(1996)124<0785:AC SOTG>2.0.CO;2.
- Zhu, M., E. B. Radcliffe, D. W. Ragsdale, I. V. MacRae, and M. W. Seeley, 2006: Low-level jet streams associated with spring aphid migration and current season spread of potato viruses in the U.S. northern Great Plains. *Agric. For. Meteor.*, 138, 192–202, https://doi.org/10.1016/j.agrformet.2006.05.001.